ROYAL SOCIETY OF CHEMISTRY

Check for updates

# MXene and MXene-based composites: synthesis, properties and environment-related applications

Xiaoxue Zhan,[a] Chen Si, [ID] ★[ab] Jian Zhou [ID] [a] and Zhimei Sun [ID] ★[ab]

In recent years, a new large family of two dimensional transition metal carbides, carbonitrides, and nitrides, so-called MXenes, have grabbed considerable attention, owing to their many fascinating physical and chemical properties that are closely related to the rich diversity of their elemental compositions and surface terminations. In particular, it is easy for MXenes to form composites with other materials such as polymers, oxides, and carbon nanotubes, which further provides an effective way to tune the properties of MXenes for various applications. Not only have MXenes and MXene-based composites come into prominence as electrode materials in the energy storage field as is widely known, but they have also shown great potential in environment-related applications including electro/photocatalytic water splitting, photocatalytic reduction of carbon dioxide, water purification and sensors, thanks to their high conductivity, reducibility and biocompatibility. In this review, we summarize the synthesis and properties of MXenes and MXene-based composites and highlight their recent advances in environment-related applications. Challenges and perspectives for future research are also outlined.

## 1 Introduction

Since the discovery of graphene in 2004, two-dimensional (2D) materials have attracted great interest.[1–4] Owing to the reduction of the dimension and size, 2D materials have exhibited many intriguing properties that are not found in their bulk counterparts, holding tremendous promise for a host of applications ranging from electronic and optoelectronic devices to electrochemical catalysis.[5–9] In recent years, with great advances in synthetic techniques, more and more 2D materials beyond graphene have been successfully produced.[10] Among them, a newly discovered large family of 2D early transition metal carbides and/or nitrides, named "MXenes", is a rapidly rising star.[11–18] MXenes are synthesized mainly by etching the A layers from the MAX phases[19–21] which are ternary carbides or nitrides with a general chemical formula $M_{n+1}AX_n$, where M stands for an early transition metal, A is a group IIIA or IVA element, X is C and/or N, and $n = 1, 2, 3$.[22] MAX phases possess layered hexagonal structures in which the $M_{n+1}X_n$ units and the A layers are alternately stacked (see Fig. 1a).[23] Because the M–X bonds are much stronger than the M–A bonds, the A layers can

[a] *School of Materials Science and Engineering, Beihang University, Beijing 100191, China. E-mail: sichen@buaa.edu.cn, zmsun@buaa.edu.cn*
[b] *Center for Integrated Computational Materials Engineering, International Research Institute for Multidisciplinary Science, Beihang University, Beijing 100191, China*

*Xiao-Xue Zhan received her BS degree from the Department of Resources and Materials, Northeastern University, China, in 2017. Now she is a graduate student studying under the advisement of Prof. Chen Si and Prof. Zhimen Sun at the School of Materials Science and Engineering, Beihang University. Her research interests are electronic and magnetic properties of two-dimensional materials.*

**Xiaoxue Zhan**

*Chen Si is an associate professor at the School of Materials Science and Engineering, Beihang University, China. She received her PhD degree in Condensed Matter Physics from Tsinghua University in 2014. Her research interests lie in materials modeling and simulation from the atomic to mesoscopic scales, with a recent focus on the properties of surfaces, interfaces and two-dimensional materials.*

**Chen Si**

be selectively chemically etched without destroying the M–X bonds, resulting in weakly bonded $M_{n+1}X_n$ layers that can be readily separated by sonication.[24] The formed 2D materials are called MXenes to stress the loss of A layers from the parent MAX phase and their 2D nature similar to that of graphene. It should be mentioned that in the etching process, the surfaces of the $M_{n+1}X_n$ units are always covered with functional groups such as oxygen ($=O$), hydroxyl (–OH) or/and fluorine (–F).[25,26] So the chemical formula of MXenes is summarized as $M_{n+1}X_nT_x$, where $T_x$ represents the surface functional groups. Experimentally, the proportions of different functional groups on the MXene surfaces are uncertain and change with the etching condition.

The versatile chemistries of MXenes endow them with plenty of intriguing mechanical, electronic, magnetic and electrochemical properties. In particular, the good flexibility of MXenes, combined with their 2D morphology and layered structures, makes it easy for MXenes to form composites with other materials, which provides an opportunity of integrating the outstanding properties of different materials in a complementary way. Therefore, not only MXenes but MXene-based composites also have attracted considerable research interest, holding great promise for many applications. Due to their high conductivity and excellent electrochemical activity, MXenes and MXene-based composites initially find applications in energy storage as high-performance electrode materials for lithium–sulfur batteries,[27–30] sodium-ion batteries[27,31,32] and supercapacitors.[33] It is remarkable that recently they have further risen to prominence in the environment-related fields. Specifically speaking, (i) they have been used as efficient catalysts or co-catalysts for electro/photocatalytic water splitting[34,35] and photocatalytic reduction of carbon dioxide ($CO_2$);[36] (ii) they can remove contaminants in water including heavy metal ions, organic dyes, eutrophic substances and nuclear waste;[37–39] (iii) they have also been applied to biosensors and gas sensors,[40,41]

exhibiting excellent performances. Although there have been a few reviews[13,14,18] about MXenes, these works are dedicated extensively to MXenes and pay little attention to MXene-based composites. Moreover, while the applications of MXenes in energy storage have been highlighted and carefully discussed in previous reviews,[11,12,15–17] the latest encouraging progress in environment-related applications of MXenes has not been summarized in detail. As environmental pollution is constantly intensified in many parts of the world, environmental protection and remediation has been a task that brooks no delay. In this context, it is highly desirable to summarize the progress of MXenes and MXene-based composites in environment-related applications.

In the following sections, we will give an overview of the most recent advances of MXenes and their composites, covering both experimental and theoretical studies. We begin with a brief review of the synthesis and processing of MXenes, then we summarize and classify the synthesized various MXene-based composites. After that, we move on to the properties and applications of MXenes and MXene-based composites. We discuss their mechanical, electronic and magnetic properties and highlight their tremendous promise in environment-related applications including catalysis, water remediation and sensors. Finally, we conclude this review with a description of the challenges and an outlook for future research in the MXene field, so as to promote more explorations of this new, but promising and quickly expanding family of materials.

## 2 Synthesis of MXenes

As summarized in Table 1, more than 20 different MXenes have been synthesized by chemically selectively etching certain atomic layers from the layered carbide, nitride, or carbonitride precursors. The etchants can be mainly divided into two

**Jian Zhou**

*Jian Zhou is an associate professor at the School of Materials Science and Engineering, Beihang University, China. He obtained his PhD from the Institute of Metal Research, Chinese Academy of Sciences in 2003. He worked at RWTH Aachen University (Germany), Royal Institute of Technology (Sweden), Xiamen University (China), before joining Beihang University. His research interests are thermoelectric materials, intermetallics and superalloys.*

**Zhimei Sun**

*Zhimei Sun is a Cheung Kong Scholar Chair Professor at the School of Materials Science and Engineering, Beihang University, China. She received her PhD in Materials Science from the Institute of Metal Research, Chinese Academy of Sciences in 2002. Before joining Beihang University, she worked at RWTH Aachen University (Germany), Uppsala University (Sweden) and Xiamen University (China). Her research interests include*

*electronic and amorphous structures of phase-change materials for random access memory, mechanical properties of high-performance structural materials and optoelectronic properties of 2D materials by experiments and computational simulations.*
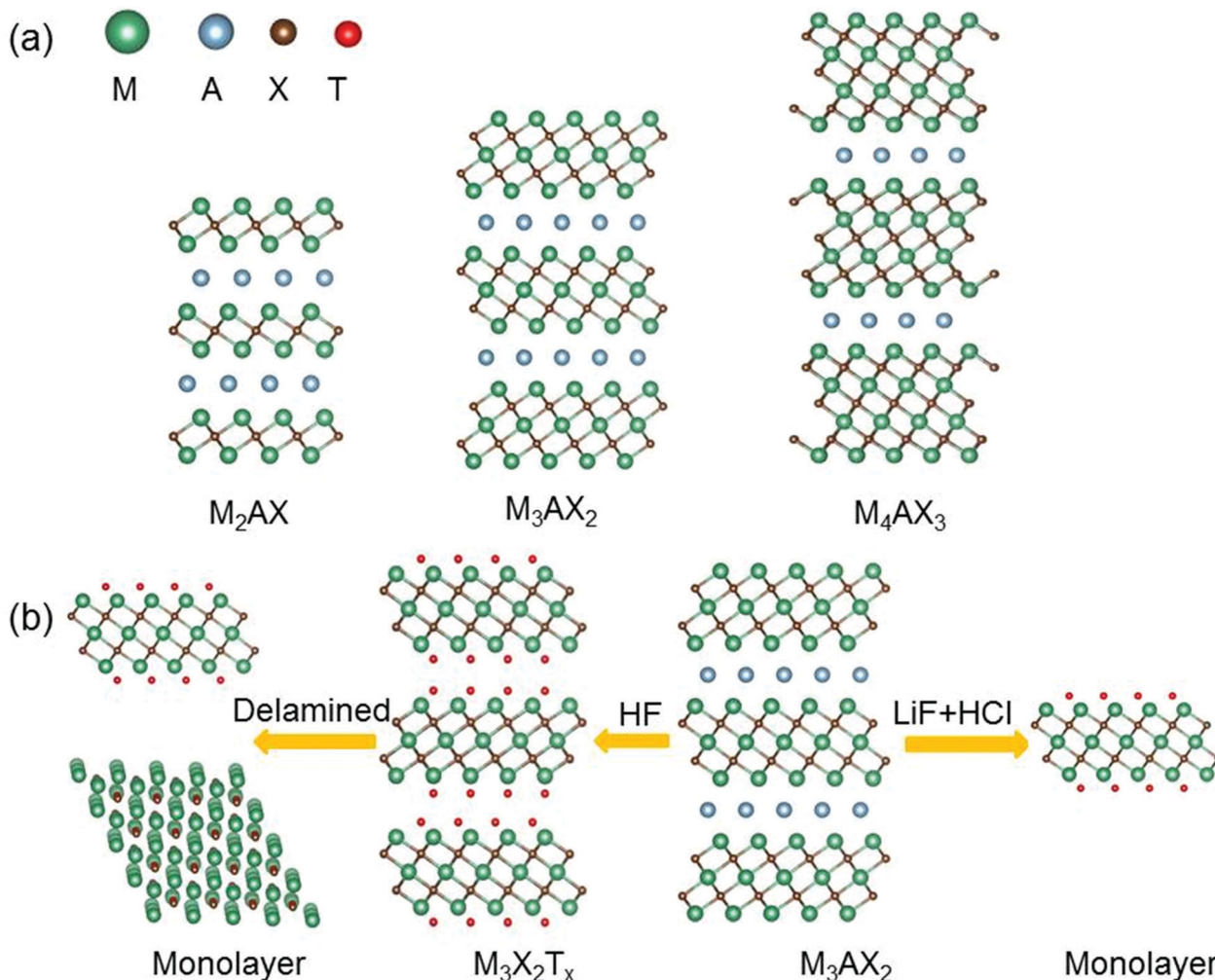
Fig. 1 (a) Crystal structures of $M_2AX$, $M_3AX_2$ and $M_4AX_3$ phases. (b) Synthesis of multilayer MXenes by HF etching or monolayer MXenes by LiF + HCl etching. Green, light blue, brown and red balls represent M (transition metal), A (mostly Al or Si), X (C or N) and T (O, F or OH), respectively.

categories: acidic solutions containing fluoride ions (HF, a mixture of LiF and HCl, or $NH_4HF_2$) and salts containing fluorine ions ($NH_3F$, KF, LiF or NaF).

Initially, MXenes are separated from MAX phases by soaking MAX phases in specific acids and destroying the M–A bonds. In this process, a certain corrosion time and full agitation are needed.

Naguib et al. synthesized the first MXene, $Ti_3C_2T_x$, by immersing $Ti_3AlC_2$[42] powders in 50% concentrated hydrofluoric acid (HF) at room temperature (RT) for 2 h.[24] Fig. 2a shows the X-ray diffraction (XRD) pattern before and after $Ti_3AlC_2$ is etched. It is clearly seen that after HF treatment the position of the main peak in the XRD pattern shifts from around 40° to around 10°, indicating that $Ti_3AlC_2$ is replaced by $Ti_3C_2T_x$. Note that the experimental XRD pattern after HF etching is similar to the simulated XRD patterns of $Ti_3C_2F_2$ and $Ti_3C_2(OH)_2$ (green and red curves in Fig. 2a), suggesting the presence of functional groups. Subsequently, this method of HF etching is successfully applied to other MAX phases, yielding many new MXenes including $Ti_2CT_x$,[43] $V_2CT_x$,[44,45] $Nb_2CT_x$,[44] $Ti_2NT_x$,[46] $(V_{0.5}Cr_{0.5})_3C_2T_x$,[47]

$(Ti_{0.5}Nb_{0.5})_2CT_x$,[47] $Mo_{4/3}CT_x$,[48] $Nb_{4/3}CT_x$,[49] $W_{4/3}CT_x$,[50] $Ti_3C_2T_x$,[51,52] $Ti_3CNT_x$,[47] $Nb_4C_3T_x$,[53] $Ta_4C_3T_x$,[47] $V_4C_3T_x$,[54] $Mo_2TiC_2T_x$,[55] $Mo_2Ti_2C_3T_x$[55] and $Cr_2TiC_2T_x$.[55]

Considering that HF is harmful to the human body and environment, it is a must to develop other harmless etchants. Ghidiu et al. used a safer mixture solution of hydrochloric acid (HCl) and lithium fluoride (LiF) in which $Ti_3AlC_2$ powders were soaked at 35 °C for 24 h to obtain $Ti_3C_2T_x$.[56] It can be seen from the transmission electron microscopy (TEM) image of $Ti_3C_2T_x$ (Fig. 2b) that the synthesized sample has fewer defects. Because the HCl and LiF mixture solution also has hydrogen and fluoride ions, we can infer that it has the same etching mechanism for the MAX phases with the HF solution. In fact, other combinations of acids ($H_2SO_4$) and salts containing fluorine ions (NaF, $FeF_3$, KF, CsF, $CaF_2$) have also been used to synthesize MXenes.[56] So far, many MXenes including $Ti_2CT_x$,[57] $Mo_2CT_x$,[58] $V_2CT_x$,[59] $W_{4/3}CT_x$,[50] $Ti_3C_2T_x$,[56] $Ti_3CNT_x$,[60] $Cr_2TiC_2T_x$[61] and $(Nb_{0.8}Zr_{0.2})_4C_3T_x$[62] and $(Nb_{0.8}Ti_{0.2})_4C_3T_x$[62] have been successfully produced by using mixture solutions of acids and salts containing fluorine ions. However, in the etching

**Table 1**  Summary of synthesized MXene

| Precursors | Mxene | Etchants | Conditions | | | |
| --- | --- | --- | --- | --- | --- | --- |
| | | | $T$ (°C) | Time (h) | Yield (%) | Ref. |
| $Ti_2AlC$ | $Ti_2CT_x$ | 10% HF | RT | 10 | 80 | 43 |
| $V_2AlC$ | $V_2CT_x$ | 50% HF | RT | 90 | 60 | 45 |
| $Nb_2AlC$ | $Nb_2CT_x$ | 50% HF | RT | 90 | 100 | 44 |
| $Ti_2AlN$ | $Ti_2NT_x$ | 5% HF | RT | 24 | NA | 46 |
| $Mo_2Ga_2C$ | $Mo_2CT_x$ | 50% HF | 50 | 3 | NA | |
| $(Ti_{0.5}Nb_{0.5})_2AlC$ | $(Ti_{0.5}Nb_{0.5})_2CT_x$ | 51% HF | RT | 28 | 80 | 47 |
| $Ti_3AlC_2$ | $Ti_3C_2T_x$ | 50% HF | RT | 2 | 100 | 24 |
| $(V_{0.5}Cr_{0.5})_3AlC_2$ | $(V_{0.5}Cr_{0.5})_3C_2T_x$ | 50% HF | RT | 69 | NA | 47 |
| $Ta_4AlC_3$ | $Ta_4C_3T_x$ | 50% HF | RT | 72 | 90 | 47 |
| $Nb_4AlC_3$ | $Nb_4C_3T_x$ | 50% HF | RT | 96 | 77 | 53 |
| $V_4AlC_3$ | $V_4C_3T_x$ | 40% HF | RT | 165 | NA | 54 |
| $Ti_3AlCN$ | $Ti_3CNT_x$ | 30% HF | RT | 18 | 80 | 47 |
| $Mo_2TiAlC_2$ | $Mo_2TiC_2T_x$ | 50% HF | RT | 48 | 100 | 55 |
| $Mo_2Ti_2AlC_3$ | $Mo_2Ti_2C_3T_x$ | 50% HF | 55 | 90 | 100 | 55 |
| $(Mo_{2/3}Y_{1/3})_2AlC$ | $Mo_{4/3}CT_x$ | 48% HF | RT | 60 | NA | 48 |
| | | 10% HF | RT | 72 | | |
| $(Nb_{2/3}Sc_{1/3})_2AlC$ | $Nb_{4/3}CT_x$ | 48% HF | RT | 30 | NA | 49 |
| $(W_{2/3}Sc_{1/3})_2AlC$ | $W_{4/3}CT_x$ | 48% HF | RT | 30 | NA | 50 |
| $Zr_3Al_3C_5$ | $Zr_3C_2T_x$ | 50% HF | RT | 60 | NA | 68 |
| $Hf_3[Al(Si)]_4C_6$ | $Hf_3C_2T_x$ | 35% HF | RT | 60 | NA | 69 |
| $Ti_2AlC$ | $Ti_2CT_x$ | 0.9 M LiF + 6 M HCl | 40 | 15 | NA | 57 |
| $Mo_2Ga_2C$ | $Mo_2CT_x$ | 3 M LiF + 12 M HCl | 35 | 384 | NA | 58 |
| $V_2AlC$ | $V_2CTx$ | 2 g LiF + 40 M HCl | 90 | 48 | NA | 59 |
| $Ti_3AlC_2$ | $Ti_3C_2T_x$ | 3 M LiF + 6 M HCl | 40 | 45 | 100 | 56 |
| $Ti_3AlCN$ | $Ti_3CNT_x$ | 0.66 g LiF + 6 M HCl | 35 | 12 | NA | 60 |
| $Cr_2TiAlC_2$ | $Cr_2TiC_2T_x$ | 5 M LiF + 6 M HCl | 55 | 42 | 80 | 61 |
| $(Nb_{0.8}Zr0.2)_4AlC_3$ | $(Nb_{0.8}Zr_{0.2})_4C_3T_x$ | LiF + 12 M HCl | 50 | 168 | NA | 62 |
| $(W_{2/3}Sc_{1/3})_2AlC$ | $W_{4/3}CT_x$ | 4 g LiF + 12 M HCl | 35 | 48 | NA | 50 |
| $Ti_3AlC_2$ | $Ti_3C_2T_x$ | 1 M $NH_4HF_2$ | 80 | 12 | NA | 63 |
| $Ti_3AlC_2$ | $Ti_3C_2T_x$ | $NH_3F$ | 150 | 24 | NA | 65 |
| $Ti_4AlN_3$ | $Ti_4N_3T_x$ | 59% KF + 29% LiF + 12% NaF | 550 | 0.5 | NA | 66 |
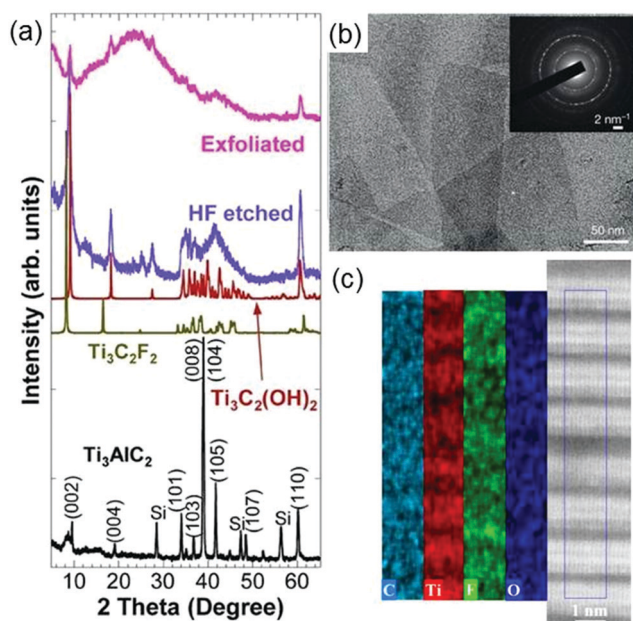


**Fig. 2** (a) XRD pattern of $Ti_3AlC_2$ before and after HF etching. Reprinted with permission from ref. 24 Copyright (2011) Wiley Online Library. (b) TEM image of lateral $Ti_3C_2T_x$. The whole selected area electron diffraction pattern is shown as the inset. Reprinted with permission from ref. 56 Copyright (2014) Nature. (c) STEM image (right panel) and EDX maps (left panel) of $Ti_3C_2T_x$. Reprinted with permission from ref. 63 Copyright (2014) American Chemical Society.

process these mixture solutions still release a few harmful HF gases.

Interestingly, Hliam *et al.* find that the weakly acidic and environmentally friendly fluoride-containing ammonium hydroxide ($NH_4HF_2$) can synthesize MXense but does not produce harmful gases.[63] Fig. 2c displays the scanning transmission electron microscopy (STEM) image and the energy dispersive X-ray spectroscopy (EDX) maps of the synthesized $Ti_3C_2T_x$. The EDX maps show the distribution of C, Ti, F, and O atoms over the STEM image, confirming the existence of terminal hydroxyl and fluoride groups on the surface of $Ti_3C_2T_x$. Moreover, it is observed that the $c$ lattice constant of $Ti_3C_2T_x$ etched by $NH_4HF$ is 25% larger than that of $Ti_3C_2T_x$ etched by HF. Subsequently, Feng *et al.* further find that the presence of surface functional groups makes the $Ti_3C_2T_x$ surface negative, hence the cations ($NH_4^+$) are attracted by the negative surface and anchored onto the surface, and the $c$ lattice parameter of $Ti_3C_2T_x$ is enlarged accordingly.[64]

It is noteworthy that in the etching process, a complete conversion of the MAX phase to MXene is required, which depends on a careful adjustment of the etching conditions. Usually, the etching conditions should be changed with the M atom and the $n$ in the chemical formula $M_{n+1}AX_n$. When the atomic number of M increases, the M–A bond energies increase and thus both the fluorine ion concentration in the etchant solution and the etching time should be increased. A larger $n$

vaule also requires a longer etching time and a larger fluorine ion concentration. Furthermore, if the etchant becomes less acidic, a higher temperature is needed. Therefore, not only the acid solutions but the salts containing fluorine ions are also able to serve as etchants for making MXenes, although the latter should be associated with a much higher etching temperature. For example, by immersing $NH_4F$ and $Ti_3AlC_2$ powders in deionized water, fully stirring, and heating isothermally at a high temperature (150 °C) for 24 h, Wang et al. have synthesized $Ti_3C_2T_x$.[65] In addition, Urbankowski et al. successfully produce the first nitride-based MXene ($Ti_4N_3T_x$) by heating a mixture of $Ti_4AlN_3$ powders and molten fluoride salts at 550 °C in an argon atmosphere.[66] The synthesis of $Ti_4N_3T_x$ provides a good example for the fabrication of other 2D transition metal nitrides.

Besides MAX phases, Zhou et al. discover that a new family of layered ternary and quaternary compounds with the formula of $M_nAl_3C_2$ or $M_n[Al(Si)]_4C_3$ can also be used as precursors to synthesize MXenes. The structure of $M_nAl_3C_2$ or $M_n[Al(Si)]_4C_3$ can be described as 2D $M_{n+1}C_n$ layers "glued" together with $(AlC)_x$ or $[Al(Si)C]_x$ untis.[67] Using this new family of compounds,

they have successfully produced $Zr_3C_2T_x$ and $Hf_3C_2T_x$. Specifically, $Zr_3C_2T_x$ is obtained by removing the $(AlC)_x$ units from $Zr_3Al_3C_5$ in 50% concentrated HF solution.[68] As disclosed by the XRD patterns (Fig. 3a), after $Zr_3Al_3C_5$ is treated with HF, the intensities of the peaks originating from $Zr_3Al_3C_5$ substantially decrease and the position of the highest peak changes from (103) to (111). Moreover, the scanning electron microscopy (SEM) image (Fig. 3b) of $Zr_3Al_3C_5$ after the HF treatment shows the exfoliation of individual Al–C layers along the basal plane, which also verifies the formation of $Zr_3C_2T_x$. The chemical reactions occurring during the etching process of $Zr_3Al_3C_5$ can be reasonably described by the following simplified equation:

$$Zr_3Al_3C_5 + HF = AlF_3 + CH_4 + Zr_3C_2 \qquad (1)$$
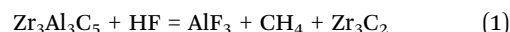
However, different from $Zr_3C_2T_x$, $Hf_3C_2T_x$ cannot be synthesized by removing $(AlC)_x$ units from $Hf_3Al_3C_5$ by HF etching, because the interfacial bonds between Hf–C and Al–C units are very strong in $Hf_3Al_3C_5$. Fortunately, by doping Si atom in $Hf_3Al_4C_6$, the interfacial bond strength between Hf–C and Al–C units is effectively reduced, enabling the synthesis of
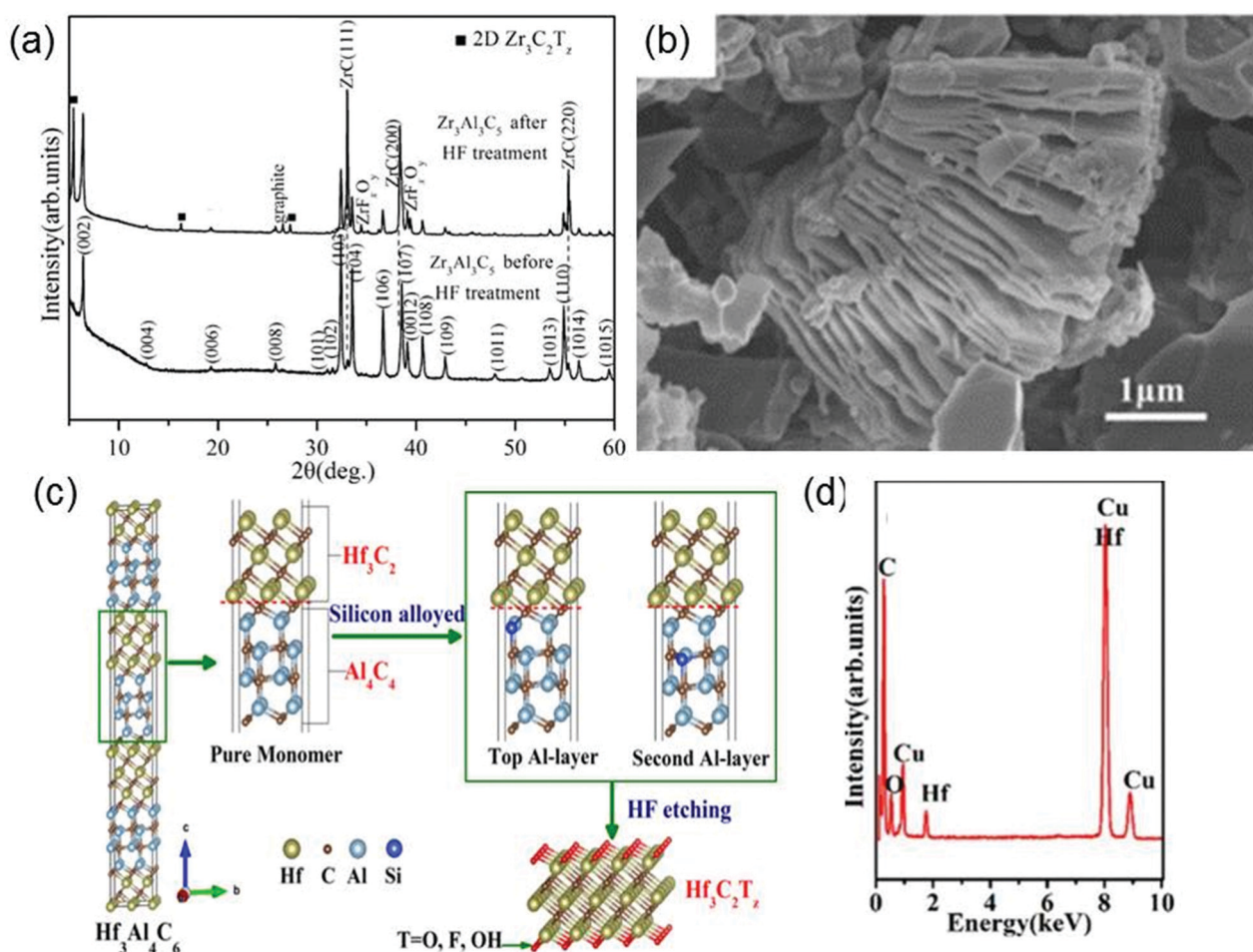


Fig. 3 (a) XRD patterns of $Zr_3Al_3C_5$ before and after HF etching. (b) SEM images of the $Zr_3Al_3C_5$ powders after HF treatment. Reprinted with permission from ref. 68 Copyright (2016) Wiley Online Library. (c) Schematic of the synthesis process of the $Hf_3C_2T_x$. (d) EDS results of the HF-etched $Hf_3[Al(Si)]_4C_6$ powders. Reprinted with permission from ref. 69 Copyright (2017) American Chemical Society.

$Hf_3C_2T_x$ from $Hf_3[Al(Si)]_4C_6$ by removing $[Al(Si)]_4C_4$ units using HF (Fig. 3c).[69] The energy dispersive spectrometer (EDS) analysis of the HF-treated $Hf_3[Al(Si)]_4C_6$ powders is shown in Fig. 3d, where not only the Hf and C signals but also the O signal appears, proving the presence of surface functional groups.

Another non-MAX phase, $Mo_2Ga_2C$, has also been reported to be able to serve as the precursor to synthesize $Mo_2CT_x$.[58,70] The structure of $Mo_2Ga_2C$ is composed of stacks of $Mo_2C$ layers interleaved with the Ga bilayers. At present, both HF[70] and LiF + HCl[58] can be used to synthesize $Mo_2CT_x$ by etching the Ga bilayers from $Mo_2Ga_2C$. This also suggests that the scope of MXene precursors could be further expanded to Ga-containing carbides and nitrides.

In general, the synthesized MXenes are usually multi-layered and need further processing to obtain a single-layer MXene.[71] Currently, there are two methods (mechanical delamination and delamination by intercalation) for delaminating multi-layered MXenes.[56] By the first method, the yield of monolayer MXenes is very low, because multi-layered MXenes have strong interlayer interactions. So far, only two research groups have successfully achieved the delamination of multi-layered $Ti_3C_2T_x$ by the mechanical layering method.[72,73] Most single-layer MXene flakes are synthesized *via* intercalation, since multi-layered MXenes can accommodate various ions and molecules between their layers.[74] The interlayer space of multi-layered MXenes is increased by intercalation, therefore, the intercalated MXenes can be converted into individual sheets by sonication in deaerated water.[71]

The intercalants can be divided into organic compounds and ionic compounds. Usually, the delamination of HF-synthesized MXenes needs organic compounds as intercalants. Organic compounds mainly include polar organic molecules, such as hydrazine, urea, isopropylamine, tetrabutylammonium hydroxide (TBAOH) and dimethyl sulfoxide (DMSO). To date, TBAOH has been successfully applied to the delamination of $Ti_3CNT_x$,[75] $Mo_2CT_x$,[58] $Ti_4N_3T_x$[66] and $V_2CT_x$,[75] and DMSO and isopropylamine have been used to delaminate $Ti_3C_2T_x$[71,76] and $Nb_2CT_x$,[29] respectively.

For multi-layered MXenes synthesized by the LiF + HCl or $NH_4F$ etchant, $Li^+$ or $NH_4^+$ ions can insert between the MXene layers.[77] Hence, these MXenes have longer $c$ lattice-parameters than HF-produced MXenes, and the corresponding monolayer MXenes can be directly obtained by sonication[76] without additional intercalation (see Fig. 1b). What's more, monolayer MXenes produced by this method have fewer defects compared to those obtained by other methods.[58]

# 3 Synthesis of MXene-based composites

In recent years, fabricating composites is an attractive strategy to develop stable and versatile materials. Due to their 2D morphology, layered structures and good flexibility, MXenes are considered as outstanding candidates for the synthesis of multifunctional composites, which has spurred a surge in the study of MXene-based composites. So far, many novel composites have been synthesized by combining MXenes with different materials including polymers, metal oxides and carbon nanotubes.

## 3.1 MXene–polymer composites

When forming composites with polymers, MXenes with excellent mechanical properties, hydrophilic surfaces, and metallic conductivity can improve the mechanical and thermal properties of polymers. In contrast to multi-layered MXenes, single-layer MXenes have higher accessible surface hydrophilicity and better compatibility with polymers. Thus, MXenes are usually delaminated before combining with polymers.

Ling *et al.* report the synthesis of a single-layered $Ti_3C_2T_x$–polyvinyl alcohol (PVA) composite by mixing the colloidal solution of $Ti_3C_2T_x$ films with a PVA aqueous solution.[78] The $Ti_3C_2T_x$–PVA composite is a layered structure where PVA is distributed between $Ti_3C_2T_x$ films (the synthesis schematic is shown in Fig. 4a). It possesses high thermostability because highly hydrophilic PVA can form strong hydrogen bonds with $Ti_3C_2T_x$. Compared with isolated $Ti_3C_2T_x$ and PVA, $Ti_3C_2T_x$–PVA has more excellent flexibility and tensile and compressive strengths. In particular, the tensile strength of the $Ti_3C_2T_x$–PVA composite with 40 wt% $Ti_3C_2T_x$ reaches 91 ± 10 MPa, which is about four times larger than that of the $Ti_3C_2T_x$ film (see Fig. 4b). In addition, $Ti_3C_2T_x$ endows this composite with high conductivity.

Naguib *et al.* synthesize a $Ti_3C_2T_x$–polyacrylamide (PAM) composite by using a two-step method.[79] First, the DMSO is introduced in the interlayers of $Ti_3C_2T_x$ to increase the layer spacing of $Ti_3C_2T_x$ and to achieve full delamination of individual $Ti_3C_2T_x$ layers. Then the prepared $Ti_3C_2T_x$ and PAM solutions are uniformly mixed and dried at ambient temperature for 4–5 days. Different $Ti_3C_2T_x$–PAM composites are prepared by varying the mass ratio of $Ti_3C_2T_x$ to PAM. When $Ti_3C_2T_x$ accounts for 6 wt%, the composite has the best mechanical properties and the highest electrical conductivity of $3.3 \times 10^{-2}$ S m$^{-1}$. As shown in the SEM fracture surface morphology image of the 6 wt% $Ti_3C_2T_x$–PAM sample (Fig. 4c), there are a large number of dimples, indicating that the fracture surface is a typical ductile fracture and this sample has good toughness.

UHMWPE (ultrahigh molecular weight polyethylene) is also reported to be able to form composites with $Ti_3C_2T_x$. Before the $Ti_3C_2T_x$–UHMWPE composite is fabricated, the surface-modified $Ti_3C_2T_x$ powders need to be prepared first, and the modified surface can improve the compatibility and dispersion stability of $Ti_3C_2T_x$ in UHMWPE.[80] The mixtures of surface-modified $Ti_3C_2T_x$ and UHMWPE are molded on a press vulcanizer, heated at a rate of 10 °C min$^{-1}$ to 220 °C and then held for 30 min under 10 MPa. The formed $Ti_3C_2T_x$–UHMWPE composites with different weights of $Ti_3C_2T_x$ have a higher strength than UHMWPE. Among them, the 10 wt% $Ti_3C_2T_x$–UHMWPE has the highest yield strength, ultimate tensile strength and elongation.[80] The mechanism for the enhancement of mechanical properties of UHMWPE by $Ti_3C_2T_x$ is displayed in Fig. 4d. As the strain is applied to the $Ti_3C_2T_x$–UHMWPE
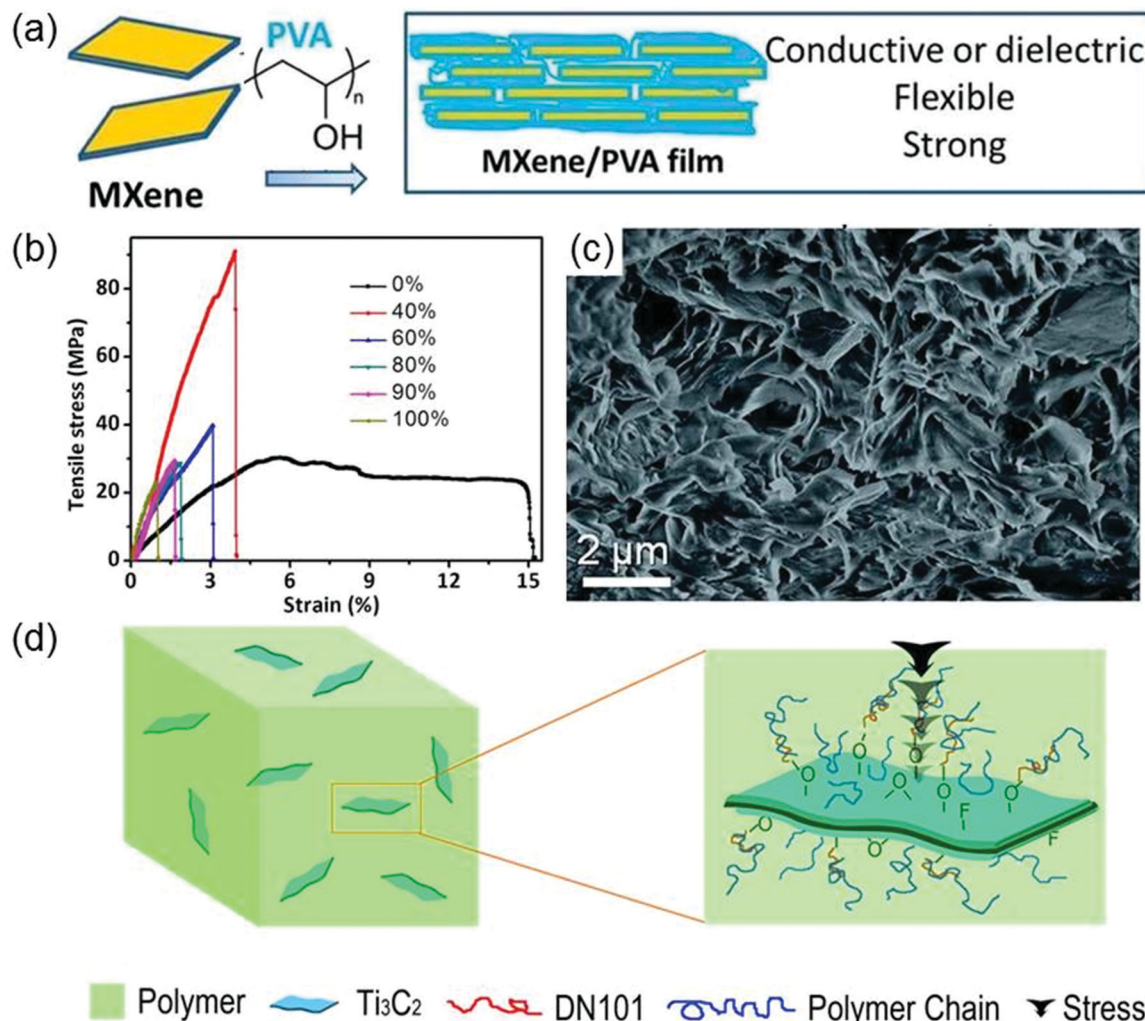
**Fig. 4** (a) Schematic for the synthesis of the $Ti_3C_2T_x$–PVA composite. (b) Stress–strain curves for $Ti_3C_2T_x$–PVA films with different $Ti_3C_2T_x$ weights. Reprinted with permission from ref. 78 Copyright (2014) PNAS. (c) SEM fracture surface morphology images of the 6 wt% $Ti_3C_2T_x$–PAM sample. Reprinted with permission from ref. 79 Copyright (2016) Royal Society of Chemistry. (d) Schematic representation of forces on the $Ti_3C_2T_x$–UHMWPE composite. Reprinted with permission from ref. 80 Copyright (2015) Elsevier.

composite, the stress on UHMWPE can be transferred to $Ti_3C_2T_x$ along the polymer chains, and the flexible $Ti_3C_2T_x$ can bear more stress than UHMWPE and effectively prevent the generation and development of cracks, accounting for the outstanding mechanical performances of this composite.

In addition to the polymers mentioned above, poly(acrylic acid),[81] polyvinylpyrrolidone (PVP),[82] poly(ethylene oxide) (PEO)[81] and alginate/PEO[81] can also form composites with MXenes. Generally, the MXene–polymer composites have better mechanical performances than the isolated MXenes and polymers. Moreover, many of them show good electric conductivity and thus are promising for applications in wearable electronic devices.

### 3.2 MXene–oxide composites

Owing to their high electrical conductivity and good electrochemical stability, MXene–oxide composites are potential electrode materials in supercapacitors and sodium- or lithium-ion batteries (LIB).[16] Zhu *et al.* synthesize $TiO_2$–$Ti_3C_2T_x$ nanocomposites in a hydrothermal

environment and use them as electrodes for electrochemical super-capacitors (Fig. 5a). The synthesis process is as follows: first, tetrabutyl titanate (TBOT) reacts with $Ti_3C_2T_x$ to form the precipitates of $TiO_2$ particles that adhere to the surface of $Ti_3C_2T_x$; then the $TiO_2$–$Ti_3C_2T_x$ nanocomposite forms by heating the sample at 500 °C for 4 hours.[83] As expected, the synthesized $TiO_2$–$Ti_3C_2T_x$ electrode exhibits a high specific capacitance and excellent cycling stability. The high electrochemical performance of the $TiO_2$–$Ti_3C_2T_x$ electrode is due to the introduction of $TiO_2$. On the one hand, $TiO_2$ particles spreading in the interlayers of $Ti_3C_2T_x$ can increase the distances between $Ti_3C_2T_x$ nanosheets to facilitate the insertion of cations; on the other hand, the presence of $TiO_2$ provides extra paths for the diffusion of electrolyte ions.

Zhang *et al.* report a layered orthorhombic $Nb_2O_5$–$Nb_4C_3T_x$ hierarchical composite which can be facilely synthesized by a one-step oxidation of $Nb_4C_3T_x$ powders in flowing $CO_2$ at 850 °C for 0.5 h.[84] A comparison of the XRD patterns of $Nb_4C_3T_x$ before and after oxidation confirms that $Nb_2O_5$ is generated on the
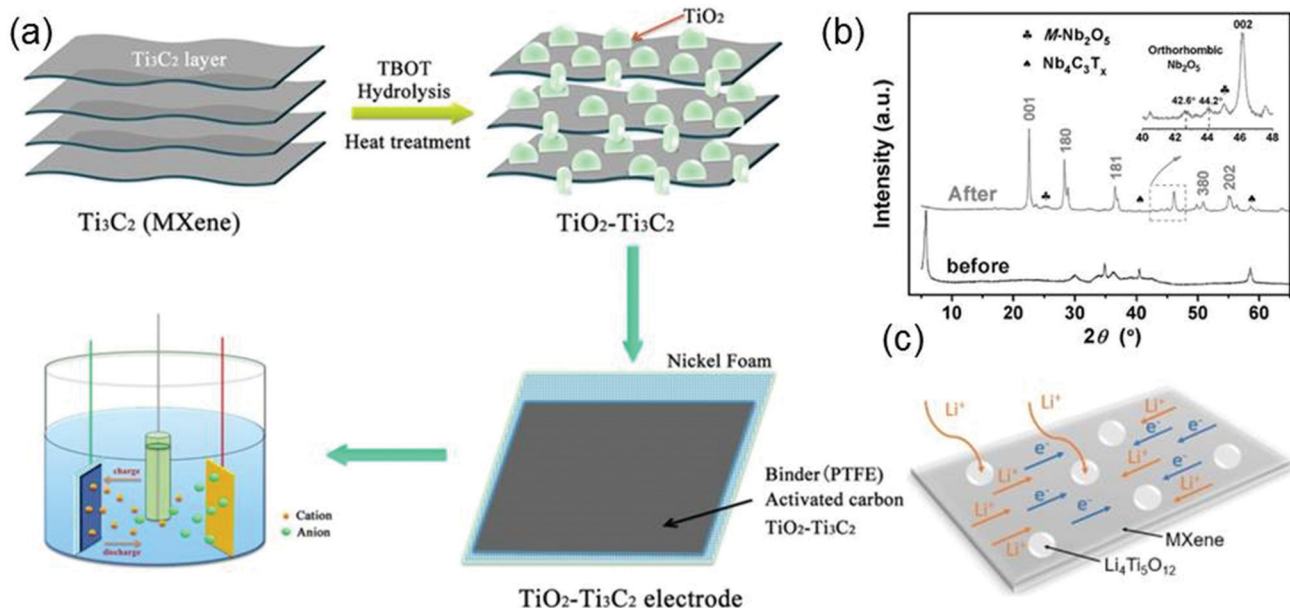
Fig. 5   (a) Procedures of hydrothermal synthesis of the $TiO_2$–$Ti_3C_2T_x$ nanocomposite. Reproduced with permission from ref. 83 Copyright (2016) ECS. (b) XRD patterns of $Nb_4C_3T_x$ before (black curves) and after (gray curves) oxidation. Reprinted with permission from ref. 84 Copyright (2016) Wiley Online Library. (c) Schematic for the ion and electron transfer in the $Li_4Ti_5O_{12}$–$Ti_3C_2T_x$ electrode. Reprinted with permission from ref. 85 Copyright (2017) Elsevier.

$Nb_4C_3T_x$ surfaces after oxidation (see Fig. 5b). In the $Nb_2O_5$–$Nb_4C_3T_x$ composite, $Nb_2O_5$ is uniformly distributed at the edges and in the interlayers of the $Nb_4C_3T_x$ sheets, effectively shortening the ion diffusion paths. Meanwhile, the internal unoxidized $Nb_4C_3T_x$ promotes the overall electronic conductivity of the composite. The above two factors are responsible for the high electrochemical and cycling performances of the $Nb_2O_5$–$Nb_4C_3T_x$ composite.

Wang et al. propose a simple strategy to obtain a $Li_4Ti_5O_{12}$–$Ti_3C_2T_x$ composite. The corresponding synthetic process is composed of two procedures. First, by mixing $Ti_3C_2T_x$, various hydrogen peroxides and $LiOH\cdot H_2O$ together in deionized (DI) water, the lithium ions can enter into the interlamination of $Ti_3C_2T_x$ to enlarge its interlayer spacing. Then the obtained products are washed using DI water several times and dried at 40 °C for 24 h, followed by calcination at 550 °C for 4 h under $N_2$ to obtain the final products.[85] The synthesized $Li_4Ti_5O_{12}$–$Ti_3C_2T_x$ composite also has excellent electrochemical properties, being considered as a promising anode material for lithium ion batteries (LIBs). Fig. 5c displays the schematic of the transfer of electrons and ions in the layered-stacked $Li_4Ti_5O_{12}$–$Ti_3C_2T_x$ composite. When the $Li_4Ti_5O_{12}$–$Ti_3C_2T_x$ electrode is soaked in the electrolyte, $Li_4Ti_5O_{12}$ with low lithium ion diffusion barriers grows on the surface of the MXene, resulting in the substantial shortening of the migration paths of lithium ions. Moreover, the high electrical conductivity of $Ti_3C_2T_x$ ensures the rapid electron transfer from the electrolyte to electrode. Consequently, the $Li_4Ti_5O_{12}$–$Ti_3C_2T_x$ electrode has fast electronic and ionic diffusion, leading to the improvement of the lithium-storage performance.

Huang et al. introduce metal oxide nanobelts into MXene to synthesize a sandwich-structured $Ti_3C_2T_x$–$Na_{0.23}TiO_2$ nanocomposite which is made of interwoven amorphous $Na_{0.23}TiO_2$ nanobelts growing on layered $Ti_3C_2T_x$ nanosheets (Fig. 6a), via a hot aqueous method.[86] This nanocomposite as an LIB anode not only exhibits an impressive cycling performance but also shows a remarkable rate capability, as shown in Fig. 6b and d. The cycling stability of $Na_{0.23}TiO_2$–$Ti_3C_2T_x$ is evaluated by performing a long cycling test on the $Na_{0.23}TiO_2$–$Ti_3C_2T_x$ electrode at 5 A g$^{-1}$ (see Fig. 6b). The discharge capacity exhibits an upward trend with an increase in the number of cycles and is finally stabilized at a high value after 4000 cycles. On the other hand, as shown in Fig. 6d, as the current density varies from 0.1 to 5 A g$^{-1}$, the reversible capacity is quite high all along, and it can still reach a large value of 288 mA h g$^{-1}$ even when the current density is suddenly returned to 0.1 A g$^{-1}$ from 5 A g$^{-1}$. This directly verifies the high rate capability of $Na_{0.23}TiO_2$–$Ti_3C_2T_x$. The above high cycling stability and rate capability of $Na_{0.23}TiO_2$–$Ti_3C_2T_x$ can be attributed to its sandwich-like structure that reduces the $Li^+/Na^+$ transfer paths and effectively releases the strain of the electrode upon cycling (see Fig. 6c).

So far, the metal oxides which have been reported to form composites with MXenes include $TiO_2$,[83] $Nb_2O_5$,[84] $Li_4Ti_5O_{12}$,[85] $Na_{0.23}TiO_2$,[86] $SnO_2$,[87] $Co_3O_4$,[88] $NiCo_2O_4$,[89] $Sb_2O_3$,[89] $Fe_3O_4$,[90] and $Cu_2O$.[91] It is clearly seen that these oxides are basically transition metal oxides (TMOs). The formed TMO–MXene composites working as electrodes of sodium- or lithium-ion batteries and supercapacitors all exhibit good performances. Among them, a spray-coated $Ti_3C_2T_x$–$NiCo_2O_4$ hybrid film electrode has the best reversible capacity (1330 mA h g$^{-1}$ at 0.1C) and cycling stability (1330 mA h g$^{-1}$ at 1C after 100 cycles).[88]

### 3.3  MXene–carbon nanotube (CNT) composites.

Zhao et al. fabricate $Ti_3C_2T_x$–CNT composites and employ them in electrochemical capacitors. Fig. 7a shows the schematic for
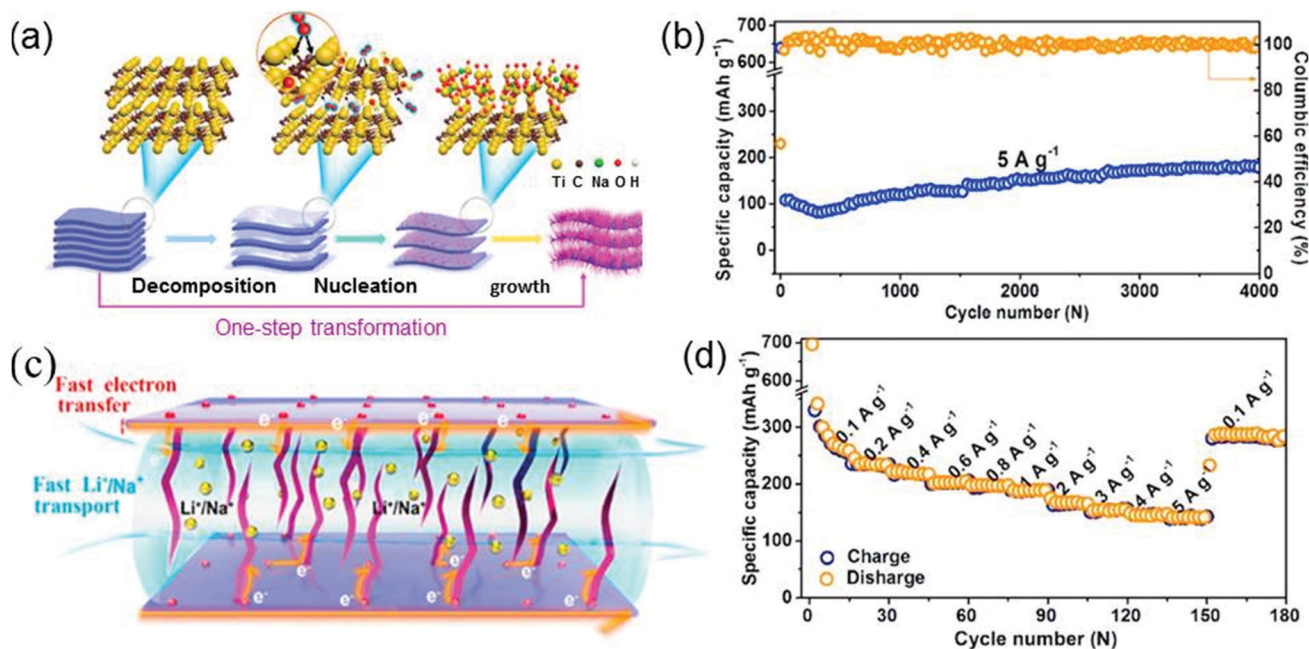
**Fig. 6** (a) Schematic diagram for the synthesis of $Na_{0.23}TiO_2–Ti_3C_2T_x$ composites by an *in situ* transformation reaction. (b) Cycling performances of $Na_{0.23}TiO_2–Ti_3C_2T_x$ composites as LIB anodes. (c) Energy-storage mechanism of $Na_{0.23}TiO_2–Ti_3C_2T_x$ in the discharge process. (d) Rate capability of $Na_{0.23}TiO_2–Ti_3C_2T_x$. Reprinted with permission from ref. 86 Copyright (2018) Elsevier.
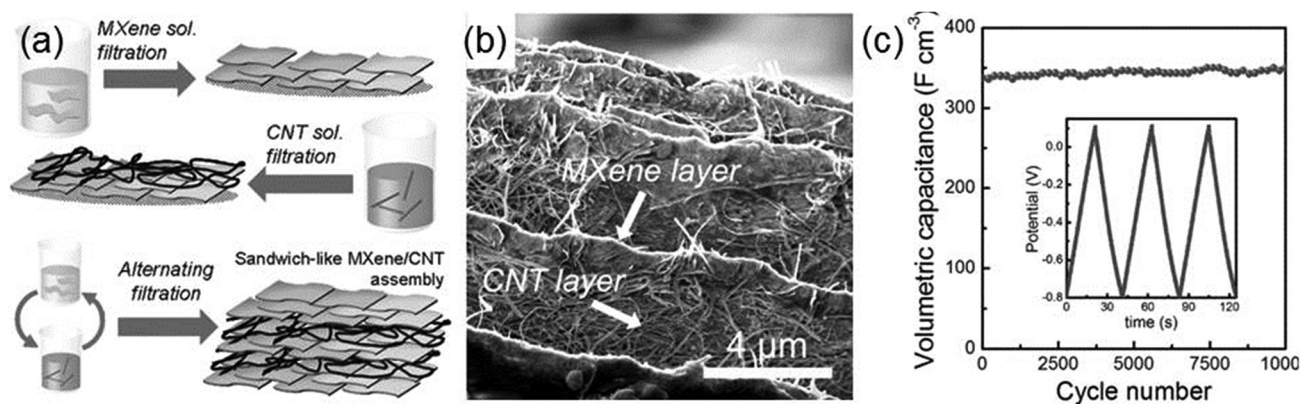


**Fig. 7** (a) Preparation of the sandwich-like $Ti_3C_2T_x–CNT$ composite. (b) Cross-sectional SEM images of $Ti_3C_2T_x–CNT$ papers. (c) Cycling stability of the $Ti_3C_2T_x–CNT$ electrode at 10 A g$^{-1}$. Reprinted with permission from ref. 92 Copyright (2015) Wiley Online Library.

the preparation of the $Ti_3C_2T_x–CNT$ composite, where $Ti_3C_2T_x$ layers and CNT layers are alternately deposited on top of each other until the total layer number reaches 6–10.[92] In the microscopic morphology of the synthesized $Ti_3C_2T_x–CNT$ composite (Fig. 7b), one can clearly see the sandwich-like superposition of the MXene and CNT layers. When acting as the electrode of the supercapacitor, the $Ti_3C_2T_x–CNT$ exhibits significantly higher volumetric capacitance and rate performance than isolated MXene. As shown in Fig. 7c, at 10 A g$^{-1}$, the volumetric capacitance of the $Ti_3C_2T_x–CNT$ electrode increases from 340 to 370 F cm$^{-3}$ after 10 000 cycles, which is about 55% higher than that of the $Ti_3C_2T_x$ electrode. The mechanism responsible for the excellent electrochemical performance of the $Ti_3C_2T_x–CNT$ composite is that the incorporation of CNT into $Ti_3C_2T_x$ enlarges the interlayer space

between the $Ti_3C_2T_x$ flakes for cation intercalations and increases the diffusion paths of electrolyte ions.

Later, the $Ti_3C_2T_x–CNT$ composites are further used in sodium- or lithium-ion batteries.[28,32] Moreover, a $Ti_3C_2T_x–CNT$ based strain sensor has also been developed, exhibiting outstanding performances including extraordinary sensitivity, high stretchability and a tunable sensing range.[93]

# 4 Properties

## 4.1 Mechanical properties

MXenes' mechanical properties strongly depend on their surface terminations. It is predicted that the O terminated MXenes have

very high stiffness, but MXenes terminated by other groups (F and OH) show lower elastic stiffness than their O-terminated counterparts.[94] This may be related to the different lattice constants of MXenes with different terminations: usually, the O-terminated MXenes have smaller lattice parameters than the F or OH terminated MXenes.[95] Compared with bare MXenes, the surface-functionalized MXenes have larger flexibility. Using $Ti_2C$ as an example, Guo *et al.* find that the functionalization would reduce the Young's modulus of $Ti_2C$, but the functionalized $Ti_2C$ can withstand a larger strain than bare $Ti_2C$ and even graphene.[96] The surface terminated groups act as a buffer layer for $Ti_2C$ under tensile deformation, slowing down the collapse of Ti layers and increasing the value of critical strain where $Ti_2C$ fractures.

The number of atomic layers in MXene, determined by $n$ in its chemical formula $M_{n+1}X_n$, also influences the mechanical properties of MXene. Yorulmaz *et al.* study the elastic constant and Young's moduli of bare MXenes by classical molecular dynamics. They find that among all $Ti_{n+1}C_n$ ($n = 1, 2, 3$), the thinnest $Ti_2C$ has the highest Young's modulus and the elastic constant of $Ti_2C$ is almost twice higher than that of $MoS_2$.[97] For the functionalized MXene, Borysiuk *et al.* show that with the decrease of $n$, the strength and hardness of $M_{n+1}X_nT_x$ gradually increase.[98]

Experimentally, it is found that the mechanical properties of MXenes are enhanced by forming composites with polymers or carbon nanotubes. By combining different types of polymers, the flexibility, toughness, and tensile and compressive strengths of MXenes can be enhanced to different degrees. For example, the $Ti_3C_2T_x$–polyvinyl alcohol (PVA) composite has excellent flexibility and large tensile and compressive strengths. In particular, the tensile strength of $Ti_3C_2T_x$–PVA composites is about four times larger than that of isolated $Ti_3C_2T_x$.[79] Moreover, $Ti_3C_2T_x$–PAM[80] and $Ti_3C_2T_x$–UHMWPE[81] are also reported to show high toughness and yield strength.

## 4.2 Electronic properties

MXenes cover various electronic properties ranging from metallicity and semiconductivity to topological insulativity, due to their high compositional diversity, various surface functionalization possibilities, and flexible thickness controllability.[99,100] Among them, all the bare MXenes and the majority of surface-functionalized MXenes are metallic. Interestingly, the calculated work functions (WFs) of metallic MXenes can vary in a very wide range, from 1.8 eV to 8 eV, as shown in Fig. 8a.[100] It is seen that the WFs of MXenes are sensitive to their surface chemistry: for a given MXene, compared with the bare surface, the OH (O) decoration always decreases (increases) its WF, whereas the F decoration displays either trend relying on the specific material. It is worth mentioning that all the OH-terminated MXenes show ultralow WFs ($< 2.8$ eV), lower than that of Sc which
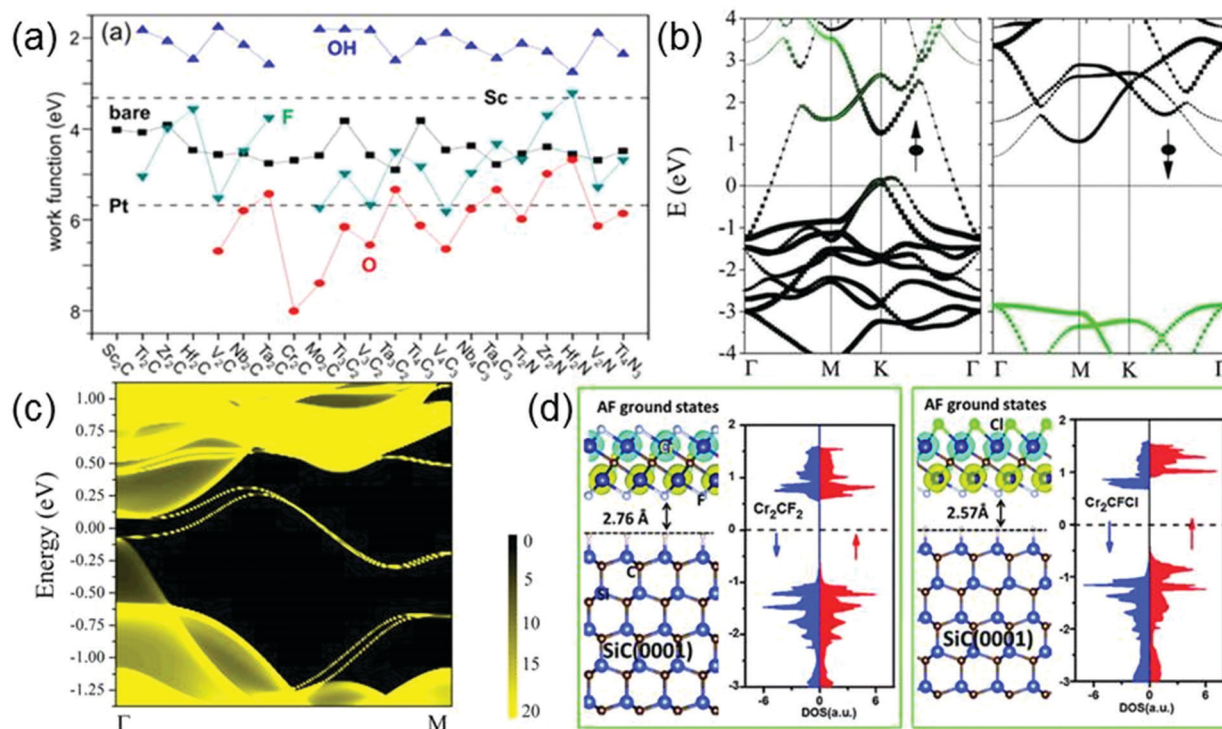


Fig. 8 (a) Work functions of MXenes with various terminations. Black squares, red circles, blue up-triangles, and cyan down-triangles are for bare, O-terminated, OH-terminated, and F-terminated MXenes, respectively. For comparison, work functions of Sc and Pt are also shown by dashed lines. Reprinted with permission from ref. 100 Copyright (2016) American Chemical Society. (b) Band structure of $Cr_2C$. Reprinted with permission from ref. 126 Copyright (2015) American Chemical Society. (c) Local density of states for $Mo_2HfC_2O_2$ on the zigzag edge. The edge states connecting the bulk valence and conduction bands form a single Dirac cone at the M point. Reprinted with permission from ref. 122 Copyright (2016) Royal Society of Chemistry. (d) Density of states of $Cr_2CF_2$ (left panel) and $Cr_2CFCl$ (right panel) supported on the SiC(0001) substrate. Reprinted with permission from ref. 130 Copyright (2016) Royal Society of Chemistry.

is nearly the lowest among those of elemental metals. On the other hand, the WFs of some O-terminated MXenes are even larger than that of Pt which has the highest WF of all elemental metals. The WFs of F-terminated MXenes always fall between those of OH- and O-terminated counterparts. The change of WF after surface functionalization comes from the change of surface dipole moment induced by functionalization.[100] The OH (O) termination always leads to a negative (positive) surface dipole moment and thus decreases (increases) WF, while F can introduce either a negative or positive surface dipole moment depending on the specific MXene material. However, it is noted that in current experiments, the mix of F, O and OH groups on the MXene surfaces usually brings the WFs of MXenes back into an intermediate value. For example, by performing Kelvin probe force microscopy analysis, Xu *et al.* determine the work function of $Ti_2C(OH)_xF_y$, which is estimated to be $\approx 4.98$ eV.[101] Therefore, to achieve the ultralow (or ultrahigh) work function of OH (or O)-terminated MXenes, a fine control of the types of the surface functional groups is indispensable.

Metallic MXenes with high/low WFs show great potential as Schottky-barrier (SB)-free metal contacts to 2D semiconductors. When MXene forms a van der Waals (vdW) heterostructure with a given 2D semiconductor, the weak interfacial vdW interaction ensures weak Fermi level pinning, which together with the high (low) work function of MXene can enable the SB-free hole (electron) injection into the 2D semiconductor. Based on first-principles calculations, it has been predicted that the OH-terminated MXenes with ultralow WFs can form n-type Schottky barrier-free contacts with common 2D semiconductors such as transition metal dichalcogenides[100,102] and blue phosphorene.[103] Among all known 2D semiconductors, $MoS_2$ has attracted the most attention, holding tremendous promise for substituting silicon in future nanoelectronics.[104] However, because the ionization energy of $MoS_2$ is as high as $\sim 6.0$ eV, it is still a great challenge to make a SB-free p-type contact to $MoS_2$. Experimentally $MoS_2$ usually displays n-type behavior when in contact with metals.[105] It is worth mentioning that in the whole MXene family, You *et al.* find six materials ($V_2CO_2$, $Cr_2CO_2$, $Mo_2CO_2$, $V_4C_3O_2$, $Cr_2NO_2$, and $V_2NO_2$) that can be used as metal contacts to $MoS_2$ with disappearing p-type Schottky barriers at $MoS_2$–MXene interfaces, leading to highly efficient hole injections into $MoS_2$.[106] This will facilitate the realization of high-performance $MoS_2$ field-effect transistors with both polarities.

Moreover, the metallicity endows many MXenes with high electronic conductivity, making them promising in many applications, particularly, as electrode materials in batteries and supercapacitors. The conductivity of MXenes ranges from smaller than 1 S cm$^{-1}$ to thousands of S cm$^{-1}$, which depends strongly on their synthesis and delamination methods. For instance, the HF-etched $Ti_3C_2T_x$ possesses a low conductivity of 2 S cm$^{-1}$,[107] but the conductivity of LiF + HCl-etched $Ti_3C_2T_x$ can reach up to 1500 S cm$^{-1}$.[108–110] Such a large difference is possibly because the former has more defects and higher F-terminations. If the LiF + HCl-etched $Ti_3C_2T_x$ is delaminated, its conductivity will be further improved.[111] In practical application, MXenes are usually combined with other promising

electrode materials (*e.g.* TMOs) to form composites which exhibit extraordinary electrochemical characteristics in lithium and sodium ion batteries and lithium–sulfur batteries. The extraordinary electrochemical performances of MXene–TMO composites are attributed to the synergistic effects of MXenes and TMO: a highly conductive MXene facilitates fast electron transport between composite materials and electrolytes; meanwhile, TMOs have rich redox reactions involving different ions that lead to a significantly higher capacity/capacitance of MXene–TMO composites than that of carbon-based electrode materials. In dozens of TMO-composites that have been synthesized, four materials which involve three distinct lithium storage mechanisms are worth mentioning. Among them, $TiO_2$–$Ti_3C_2T_x$ is based on an intercalation/deintercalation mechanism[112] and $SnO_2$–$Ti_3C_2T_x$ relies on an alloying/dealloying mechanism,[112] while $Fe_3O_4$–$Ti_3C_2T_x$ and $Co_3O_4$–$Ti_3C_2T_x$ both utilize a unique "conversion reaction" mechanism[113–115] in which the oxidation state of high-valence Co/Fe can effectively store Li-ions.

Some MXenes with specific surface functionalizations, such as $Sc_2CO_2$,[116] $Sc_2CF_2$,[116] $Sc_2C(OH)_2$,[116] $Ti_2CO_2$,[117] $Zr_2CO_2$,[118] $Hf_2CO_2$,[118] $Cr_2CF_2$[119] and $Cr_2C(OH)_2$,[119] are semiconductors, and a handful of MXenes, including $W_2CO_2$,[120] $M'_2M''C_2O_2$ ($M'$ = Mo, W and $M''$ = Ti, Zr, Hf)[121–123] and $Ti_3N_2F_2$[124] are even predicted to be 2D topological insulators (TIs). 2D TIs are a new class of materials with an insulating gap in the bulk and gapless states at the edge. Remarkably, the scatterings of the edge states are completely forbidden, leading to a dissipation-less charge or spin transport. Fig. 8c shows the local density of states of $Mo_2HfC_2O_2$ on its zigzag edge, where one can clearly see that a pair of topological edge states connects the bulk conduction and valence bands and forms a single Dirac cone at the $M$ point.[122] However, so far neither semiconducting nor topological insulating states in MXenes are realized experimentally. This is because by the present synthesis procedures, the obtained MXenes all have mixed terminations; however, the predicted superconducting and topological states basically require a single type of termination on the MXene surfaces. A control over surface chemistry of MXenes would be a key to obtaining semiconducting or topological insulating MXenes.

### 4.3 Magnetic properties

Although many 2D materials have been found, the majority of them are nonmagnetic, which limits their applications in spintronics. Therefore, the pursuit of controlled magnetism in 2D material has been a long-sought goal. Interestingly, some pristine MXenes, such as $Ti_2C$, $Ti_2N$, $Cr_2C$, $Cr_2N$ and $Mn_2C$, are predicted to be intrinsic magnetic materials. Among them, $Ti_2C$,[127] $Ti_2N$[125] and $Cr_2C$[126] are ferromagnetic, while $Cr_2N$[127] and $Mn_2C$[128] are antiferromagnetic. In particular, recently increasing attention has been paid to magnetic MXenes with half-metallicity. In half-metals, one spin-channel is metallic, while another spin channel is semiconducting, resulting in completely spin-polarized electrons at the Fermi level. $Cr_2C$ is the first predicted half metal in the MXene family.[126] Its band structure is shown Fig. 8b, where one can obviously observe a metallic spin-up channel and an insulating spin-down channel.

Moreover, its half-metallic gap, the difference between the Fermi level and the maximum of the occupied spin-down band, is as large as about 2.9 eV, indicating that the 100% spin-filter efficiency can be preserved in a broad bias range. Subsequently, the half metallicity has also been predicted in $Ti_2C$ and $Ti_2N$.[125]

The magnetic and electronic properties of bare MXenes can be easily modulated by surface functionalization. Because the magnetisms of bare MXenes usually come from the unpaired electrons of the surface transition metal atoms, upon surface passivation, the magnetisms of most MXenes will be suppressed. It is remarkable that Cr- and Mn-containing MXenes are exceptions whose magnetic moments don't disappear after surface functionalization. However, their magnetic couplings and electronic structures would be affected by functional groups. For example, when $Cr_2C$ is functionalized by F, H, OH or Cl groups, it will be transformed from a ferromagnetic half metal into an antiferromagnetic semiconductor with a sizeable band gap.[115] In contrast to $Cr_2C$, after surface passivation by O,[127] $Cr_2N$ changes from an antiferromagnetic metal to a ferromagnetic half metal. Given that $Cr_2NO_2$ displays half-metallicity in its surface-passivated form, its half-metallicity may be achieved relatively easily from the experimental point of view. For Mn-based MXenes, unterminated $Mn_2C$ is an anti-ferromagnetic metal, whereas $Mn_2CCl_2$ is an antiferromagnetic insulator and $Mn_2CF_2$ even becomes a ferromagnetic half metal with a high Curie temperature, a large half metallic gap and a sizeable magnetic anisotropy.[129]

Besides the symmetrical surface terminations mentioned above, the influences of the asymmetrical functionalization on MXenes have also been extensively investigated. It is predicted that $Cr_2CXX'$ (X, X' = H, F, Cl, Br, OH) including $Cr_2CFCl$, $Cr_2CClBr$, $Cr_2CHCl$, $Cr_2CHF$, and $Cr_2CFOH$ (corresponding to $Cr_2C$ with top and bottom surfaces asymmetrically terminated by different functional groups) are all antiferromagnetic semiconductors with Néel temperatures of about 400 K.[130] Apparently, asymmetrical functionalization induces the same ferromagnetic–antiferromagnetic transition in $Cr_2C$ as the symmetrical functionalization. However, it will introduce some additional changes on the electronic structure of $Cr_2C$, compared with the symmetrical functionalization. Fig. 8d shows the density of states (DOS) of $Cr_2CF_2$ (left panel) and $Cr_2CFCl$ (right panel). Different from the DOS of $Cr_2CF_2$ with symmetrical distribution, $Cr_2CFCl$ presents the feature of bipolar magnetic semiconductors, i.e., the VBM and CBM possess opposite spin polarizations. Similar bipolar magnetic properties are also found in other $Cr_2CXX'$, making them good candidates for spintronic applications.[130]

# 5 Environment-related applications

## 5.1 Catalysis

As the global air pollution is constantly increasing and the energy crises continue to be aggravated,[131] efficient clean energy conversion technologies such as electrochemical water splitting,[132] photocatalytic water splitting and photocatalytic

reduction of $CO_2$ are becoming of great significance. High-performance catalysts are crucial for the successful implementation of these technologies. Given that the applications of traditional catalysts including precious metals and precious-metal-based oxides (Pt,[133] $RuO_2$[134] and $IrO_2$[135]) are limited by their scarcity and high cost, developing efficient catalysts which not only have high performances but also are cost-effective is indispensable for clean energy conversion technologies. As a class of novel materials with high electronic conductivity, good surface hydrophilicity and abundant exposed metal sites, MXenes and their composites have been used in electrochemical water splitting as highly active electrode materials (electrocatalysts) as well as in photocatalytic water splitting and photocatalytic reduction of $CO_2$ as catalysts or co-catalysts, exhibiting tremendous possibilities for replacing precious metal materials.

**5.1.1 Electrocatalysis.** The water splitting reaction is divided into two half-reactions: the oxygen evolution reaction (OER) and the hydrogen evolution reaction (HER). For the former, new electrocatalysts such as graphitic carbon nitride (g-$C_3N_4$),[136–138] metal–organic frameworks (MOFs)[139–143] and layered double hydroxides (LDHs)[144–147] have been developed to replace precious metals. However, due to their poor electrical conductivity, these new catalysts mentioned above exhibit relatively low electrocatalytic performances in the OER. Combining the highly conductive materials with the above-mentioned new electrocatalysts to form composites is a promising strategy to improve their electrocatalytic performances. It has been proposed that MXenes with superior conductivity are ideal candidates for conductive supports.

The electrocatalytic activity of g-$C_3N_4$ is significantly increased by combining g-$C_3N_4$ with $Ti_3C_2T_x$ to form a composite film $Ti_3C_2T_x$–g-$C_3N_4$ (TCCN) with hydrophilic surfaces and conductive frameworks.[148] The highly flexible TCCN film has a size of a few centimeters and a thickness of 8–10 μm (see the inset of Fig. 9a), with plenty of large pores ranging from tens to hundreds of nanometers distributed in the interlayers of the film (Fig. 9a). $Ti_3C_2T_x$ not only provides a high conductivity but also forms $Ti–N_x$ units with g-$C_3N_4$ in the TCCN composite. Fig. 9b shows the polarization curves of TCCN, $Ir_2O/C$ ($IrO_2$ supported on carbon powders), $Ti_3C_2T_x$ and g-$C_3N_4$. It is seen that the anodic current recorded on TCCN has a sharp increase at 1.44 V and even exceeds that of $IrO_2/C$ at potentials beyond 1.54 V, which indicates that the TCCN has a very high OER response and catalytic activity. Moreover, after 5000 cycles, the polarization curve of TCCN is almost unchanged, revealing the good stability of TCCN.[148] Note that in addition to the high conductivity of TCCN, the hierarchical pores and the specific $Ti–N_x$ units in TCCN also make significant contributions to the excellent catalytic performance of TCCN. The hierarchical pores can achieve rapid transport of reactants and reaction products, and the $Ti–N_x$ units act as electroactive sites for reactants.

Designing metal–organic frameworks, MOFs, which involves the assembly of organic ligands and metal ions or clusters, is a potential approach to develop new excellent electrocatalysts for the OER. Generally, MOFs have porous structures, abundant
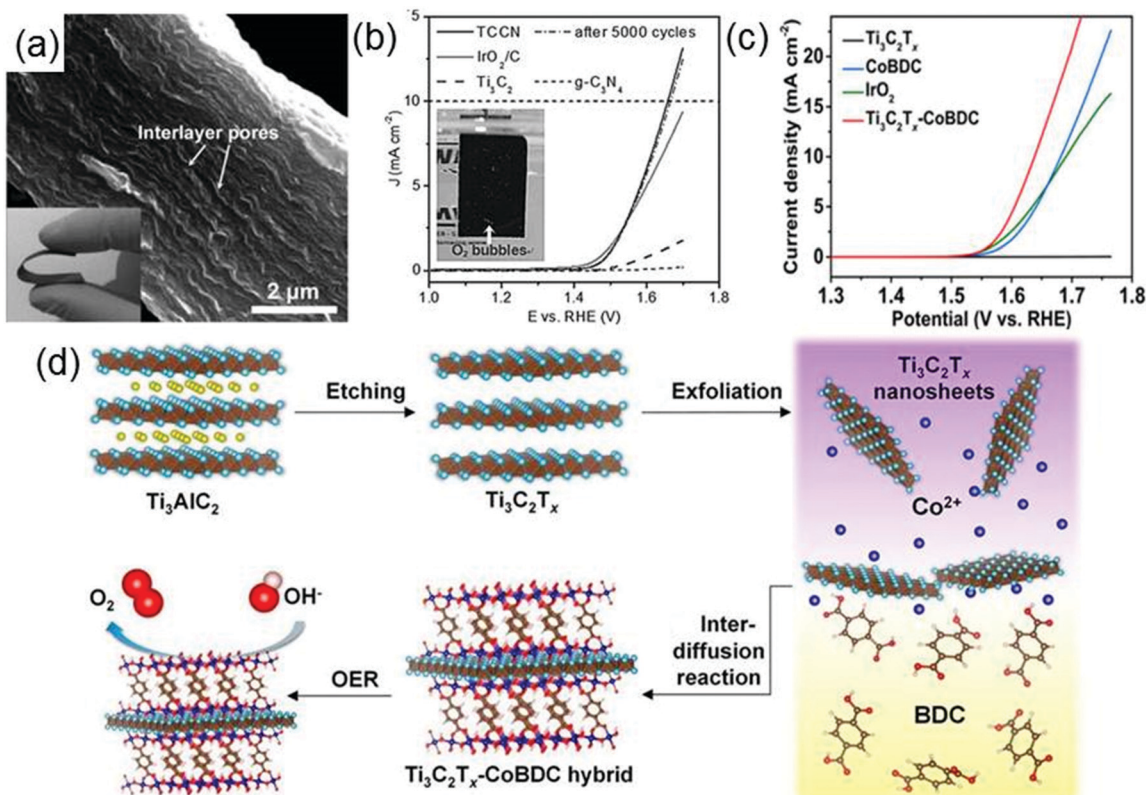
Fig. 9 (a) SEM and optical (inset) images of TCCN. (b) Polarization curves of TCCN, IrO$_2$/C, Ti$_3$C$_2$T$_x$, and g-C$_3$N$_4$. The inset is the optical image of TCCN directly used as the OER electrode with generated bubbles on the surface suggesting the formation of O$_2$. Reprinted with permission from ref. 148 Copyright (2016) Wiley Online Library. (c) OER polarization curves of glassy carbon electrodes modified with Ti$_3$C$_2$T$_x$, CoBDC, IrO$_2$, and the Ti$_3$C$_2$T$_x$–CoBDC hybrid. (d) Schematic illustration of the preparation process of the Ti$_3$C$_2$T$_x$–CoBDC hybrid for the OER. Reprinted with permission from ref. 149 Copyright (2017) American Chemical Society.

exposed active metal centers but poor electrical conductivity. Hence, the combination of MOFs with a conductive material is anticipated to improve the electrocatalytic performance of MOFs in the OER. Based on this idea, a novel MXene–MOF composite, Ti$_3$C$_2$T$_x$–CoBDC (cobalt 1,4-benzenedicarboxylate), is synthesized *via* an interdiffusion-mediated strategy (see Fig. 9d).[149] It exhibits remarkably strong electrocatalytic activity for the OER. As indicated by the linear-sweep voltammetry measurements of different catalysts deposited on glassy carbon (GC) electrodes (Fig. 9c), the current density of Ti$_3$C$_2$T$_x$–CoBDC can reach 10 mA cm$^{-2}$ at a potential of 1.64 V (*vs.* reversible hydrogen electrode, RHE), higher than those of both IrO$_2$ and CoBDC at the same potential. Similarly, a hybrid of a MOF derivative NiCoS and Ti$_3$C$_2$T$_x$ is also reported to have strong electrocatalytic activity for the OER. Strong interactions are formed between NiCoS and Ti$_3$C$_2$T$_x$, responsible for the high conductivity and efficient electron transfer in the NiCoS–Ti$_3$C$_2$T$_x$ composite.[150]

Due to the large redox activity, LDHs containing positively charged metal hydroxide layers and charge-compensating anions (*e.g.*, NO$^{3-}$, CO$_3$$^{2-}$, *etc.*) hold great promise as alternatives of noble metal electrocatalysts for the OER. However, intrinsically poor conductivity and limited electrochemically active surfaces restrict the application of LDH in the OER.

Yu *et al.* attempt to solve this problem by combining highly conductive MXenes with LDH. They fabricate a FeNi-LDH/Ti$_3$C$_2$T$_x$ composite with a structure of interconnecting porous networks as a new OER electrocatalyst that exhibits large activity for the OER.[151] Strong electronic coupling and interfacial interaction between FeNi-LDH and Ti$_3$C$_2$T$_x$ are the main factors guaranteeing the good electrocatalytic performance of this composite. Moreover, the OER catalytic performance of FeNi-LDH/Ti$_3$C$_2$T$_x$ electrocatalysts can be further improved by coating the electrode with nickel foam (NF).

Besides being used as conductive materials to improve the activity of existing catalysts, MXenes have also shown potential as new electrocatalysts for the HER. MoS$_2$ is the first 2D material identified as a promising HER catalyst. However, only the exposed edge sites of MoS$_2$ are catalytically active but its basal plane is inert, thus complex design is required to maximize the edge sites. Seh *et al.* report that MXenes can also be used as electrocatalysts for the HER based on both theoretical calculations and experiments.[152] By calculating the expected overpotential and hydrogen adsorption free energy ($\Delta G_H$) of a series of M$_2$XT$_x$ (M = Mo, Sc, Ti, Zr, Hf, and V) materials, they predict that Mo$_2$CT$_x$ is the most effective electrocatalyst. Moreover, unlike MoS$_2$, Mo$_2$CT$_x$ has a large number of catalytic sites on its basal plane. To evaluate the

real electrocatalytic performances of MXenes for the HER, a linear-sweep voltammetry measurement is performed by using glassy carbon as the substrate electrode. As shown in Fig. 10a, $Mo_2CT_x$ requires a much lower overpotential (283 mV) to reach the current density of 10 mA cm$^{-2}_{geo}$ during the initial sweep, compared with $Ti_2CT_x$ that needs a 609 mV overpotential, indicating that $Mo_2CT_x$ has a higher electrocatalytic activity than $Ti_2CT_x$. On the other hand, the $Mo_2CT_x$ curve exhibits a smaller change after continuing cycling than the $Ti_2CT_x$ curve, indicating that $Mo_2CT_x$ is a rather stable catalyst for the HER.[152]

As metal atoms cover a large proportion of the MXene surfaces, MXenes suffer poor oxygen resistance in oxygen-containing electrolytic solution, which dramatically influences the stability of MXenes as electrocatalysts and thus restricts the applications of MXenes. In order to enhance the oxygen resistance, Wu *et al.* introduce a nanoplating strategy to successfully synthesize hierarchical $MoS_2$–$Ti_3C_2T_x$@C (Fig. 10c).[153] The carbon cover on the surface of $Ti_3C_2T_x$ ($Ti_3C_2T_x$@C) can effectively suppress the surface oxidation, thus strengthening the stability of $Ti_3C_2T_x$. Moreover, the bifunctional activity of $MoS_2$ towards both Li storage and HER increases the possibility of multi-field applications of $MoS_2$–$Ti_3C_2T_x$@C. It has been found that this hierarchical structure composed of $MoS_2$ and $Ti_3C_2T_x$@C shows an excellent electrocatalytic performance for the HER. Fig. 10b shows that $Ti_3C_2T_x$@C only requires a small overpotential of 135 mV to reach the current density of 10 mA cm$^{-2}$, which is lower than those for $MoS_2$–rGO@C and $Ti_3C_2T_x$@C. Such a low value of overpotential verifies the high electrocatalytic activity of $MoS_2$–$Ti_3C_2T_x$@C. In addition, after 2000 cycles of cyclic voltammetry, there is no significant shift in

the polarization curve of the $MoS_2$–$Ti_3C_2T_x$@C electrode, indicating that $MoS_2$–$Ti_3C_2T_x$@C also has good stability.

Recently, researchers have further confirmed that MXenes composites ($Ni_2P$–$Cr_2CT_x$,[34] CoP@3D-$Ti_3C_2T_x$[154] and $Ni_{0.7}Fe_{0.3}PS_3$–$Ti_3C_2T_x$[155]) can act as bifunctional electrocatalysts toward OER and HER by both theoretical predictions and experimental verifications. Moreover, the synthesized CoP@3D–$Ti_3C_2T_x$[154] and $Ni_{0.7}Fe_{0.3}PS_3$–$Ti_3C_2T_x$[155] both have high electrocatalytic activity which even surpasses those of the traditional bifunctional electrocatalysts $RuO_2$ and Pt.

**5.1.2 Photocatalysis.** The creation of photocatalysis technologies has made photocatalytic water splitting possible. Compared to electrochemical water splitting, using solar energy to directly split water *via* a semiconductor photocatalyst avoids the utilization of other energy sources. At present, the focus of photocatalytic water splitting still mainly lies in the development of novel photocatalysts that should be inexpensive, stable and could work efficiently with visible light.

MXenes have been regarded as promising candidate catalysts for photocatalytic hydrogen production reactions. By *ab initio* calculations, Guo *et al.* have found two suitable photocatalysts ($Zr_2CO_2$ and $Hf_2CO_2$) in the MXene family for the photocatalytic hydrogen production reaction.[35] The electrical structure features of a material, including the band gap size, the positions of the conduction band minimum (CBM) and the valence band maximum (VBM), are usually used as the descriptors characterizing the feasibility of this material as a photocatalyst. Specifically, for the photocatalytic hydrogen production reactions, the band gap value of the photocatalyst should be between 1.55 and 3.0 eV. Moreover, its CBM should be higher than the hydrogen reduction potential of $H^+$/$H_2$ and its VBM should be lower than the water
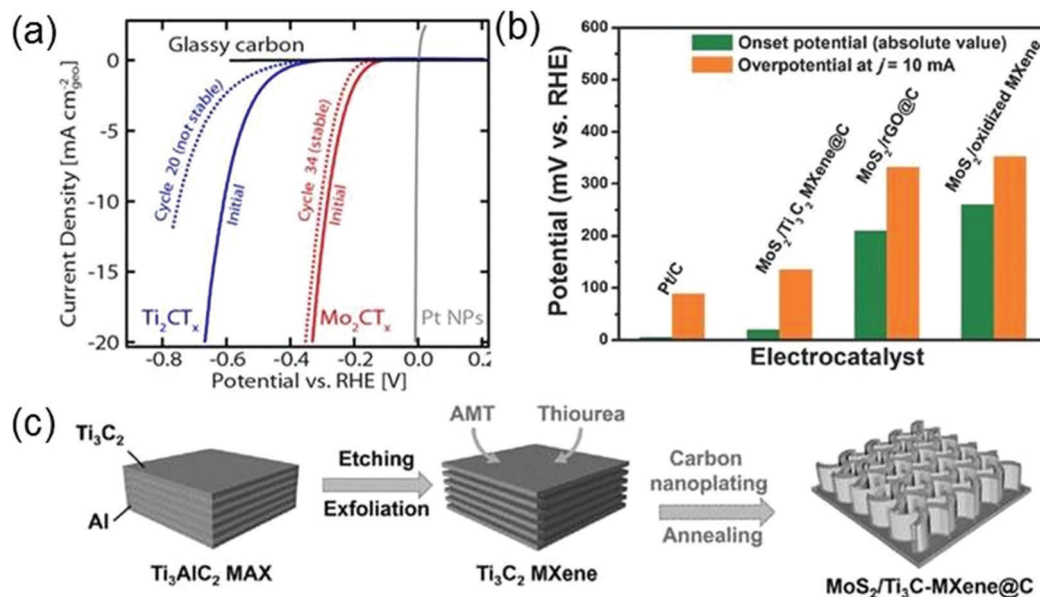


**Fig. 10** (a) Anodic-going iR-LSVs of $Ti_2CT_x$ and $Mo_2CT_x$ (mass loading: 0.1 mg cm$^{-2}_{geo}$ on glassy carbon), compared with that of bare glassy carbon. Reprinted with permission from ref. 152 Copyright (2016) American Chemical Society. (b) Comparison of Pt/C, $MoS_2$–$Ti_3C_2T_x$@C, $MoS_2$–rGO@C, and $MoS_2$/oxidized $Ti_3C_2T_x$ catalysts in terms of onset potential and overpotential at 10 mA cm$^{-2}$ (c) The synthesis procedures for $MoS_2$–$Ti_3C_2T_x$@C nanohybrids. Reprinted with permission from ref. 153 Copyright (2017) Wiley Online Library.

Fig. 11 (a) Electronic band edge positions of various MXenes relative to the water redox potential levels. (b) Optical adsorption of $Zr_2CO_2$ and $Hf_2CO_2$. Reprinted with permission from ref. 35 Copyright (2016) Royal Society of Chemistry.

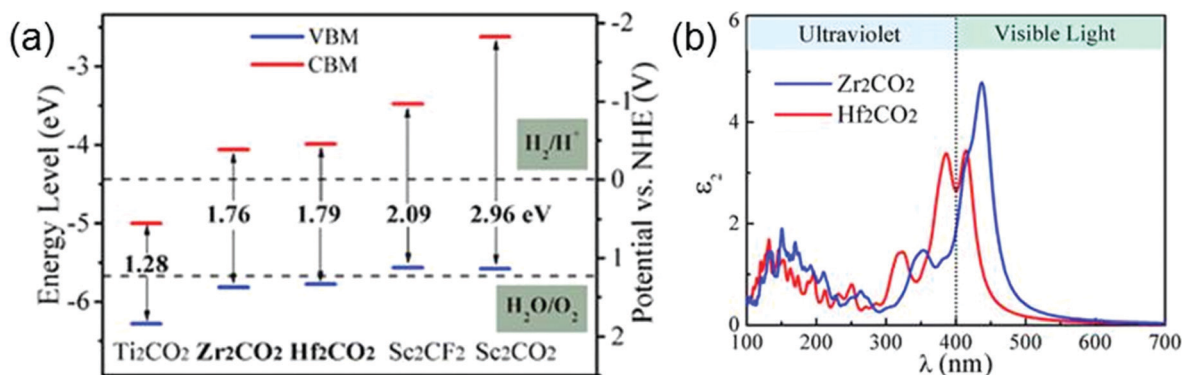oxidation potential of $H_2O/O_2$. As shown in Fig. 11a, $Zr_2CO_2$ and $Hf_2CO_2$ meet these criteria. Additionally, a favorable photocatalyst should be able to efficiently utilize the solar energy. In Fig. 11b, one can see that both 2D $Zr_2CO_2$ and $Hf_2CO_2$ display large optical absorption in the visible light region, guaranteeing the feasibility of $Zr_2CO_2$ and $Hf_2CO_2$ used as photocatalysts in water splitting reactions for producing hydrogen.[35]

Besides developing new catalysts, considerable attention has been paid to explore new ways to enhance the catalytic performances of existing photocatalysts. In recent years, co-catalysts have shown great success in boosting both the activity and the stability of photocatalysts. An outstanding co-catalyst should have the following characteristics: (i) plentiful surface functionalities to establish strong connections with the photocatalyst for perennial stability and rapid interfacial charge transfer; (ii) sufficient contacts with water molecules; (iii) a high conductivity to ensure efficient charge transport. Remarkably, MXenes can meet all the above requirements for co-catalysts. First, MXenes possess hydrophilic functional groups (–OH and –O) on their surfaces, enabling them to easily form strong interactions with various semiconductor photocatalysts and water molecules. Second, excellent electrical conductivities of MXenes guarantee efficient electron shuttling. Therefore, there has been increasing interest in exploring MXenes as co-catalysts for photocatalysts.

Ran *et al.* reveal the potential of $Ti_3C_2T_x$ as a highly efficient co-catalyst for $H_2$ evolution.[156] By rationally integrating $Ti_3C_2T_x$ nanoparticles with a chosen photocatalyst CdS *via* a hydrothermal strategy, extremely large visible-light photocatalytic $H_2$ production activity of 14 342 $\mu$mol $h^{-1}$ $g^{-1}$ is achieved, exceeding that of CdS by an incredible factor of 137. By contrast, isolated $Ti_3C_2T_x$ nanoparticles display no activity towards photocatalytic hydrogen production, indicating its role as a co-catalyst rather than as a photocatalyst. It is remarkable that $Ti_3C_2T_x$-loaded CdS also shows a higher quantum efficiency of 40.1% at 420 nm than other noble-metal free CdS-based photocatalysts reported to date including Ni–CdS, Ni(OH)$_2$–CdS, graphene-oxide–CdS and so on. The high performance of $Ti_3C_2T_x$-loaded CdS can be mainly attributed to the following two points. First, the deposition of $Ti_3C_2T_x$ on CdS enhances charge separation and

suppresses charge recombination. Under light irradiation, the photo-excited electrons on the conduction band of CdS can immediately migrate to $Ti_3C_2T_x$ because the Fermi level of $Ti_3C_2T_x$ is energetically lower than the conduction band of CdS. Then the electrons can further rapidly move to the surface active sites of $Ti_3C_2T_x$, thanks to the excellent conductivity of $Ti_3C_2T_x$. Second, the number of O terminations on the $Ti_3C_2T_x$ surface, as the effective active sites, is greatly increased by the hydrothermal treatment which makes a large number of F terminations exchanged into O terminations. Due to the similar mechanisms, $Ti_3C_2T_x$ nanoparticles can as also act as an efficient HER co-catalyst on $Zn_xCd_{1-x}S$ or ZnS.[156]

Considering the synergistic effects of different co-catalysts, two or more co-catalysts have been combined to explore more efficient co-catalytic systems. For example, using $Ti_3C_2T_x$ nanoparticles and Pt nanoclusters as dual co-catalysts for photocatalyst g-$C_3N_4$,[157] the photocatalytic hydrogen production activity of g-$C_3N_4$ is increased to 5100 mol $h^{-1}g^{-1}$, far higher than that of g-$C_3N_4$ with Pt or $Ti_3C_2T_x$ used separately as the co-catalyst. This exceptional activity in the hybrid of g-$C_3N_4$, $Ti_3C_2T_x$ and Pt is ascribed to the fast interfacial charge transfer from g-$C_3N_4$ to $Ti_3C_2T_x$ and to Pt, leading to the effective separation of photo-generated carriers.

The photocatalytic $CO_2$ reduction reaction can produce hydrocarbon solar fuels that are advantageous to the alleviation of energy crisis and air pollution. MXene can also serve as a co-catalyst in photocatalytic $CO_2$ reduction. For instance, the surface alkalinized $Ti_3C_2T_x$ ($Ti_3C_2T_x$–OH) as a co-catalyst has been employed to enhance the photoactivity of titania (P25) in photocatalytic $CO_2$ reduction.[36] As the mass ratio of $Ti_3C_2T_x$–OH to P25 varies to 5%, the evolution rates of CO and $CH_4$ reach the maximum values, 11.74 and 16.61 $\mu$mol $g^{-1}$ $h^{-1}$, respectively (see Fig. 12a), which are apparently higher than those of P25, Pt–P25 and $Ti_3C_2T_x$–P25, indicating that the photocatalytic activity of P25 has been considerably boosted by using $Ti_3C_2T_x$–OH as the co-catalyst. The excellent performance of $Ti_3C_2T_x$–OH can be ascribed to the increase of the number of hydroxyl groups on $Ti_3C_2T_x$ surfaces providing sufficient sites for $CO_2$ adsorption.

Cao *et al.* successfully prepare 2D heterojunctions of ultra-thin $Ti_3C_2T_x$–$Bi_2WO_6$ nanosheets ($Bi_2WO_6$ is the photocatalyst,
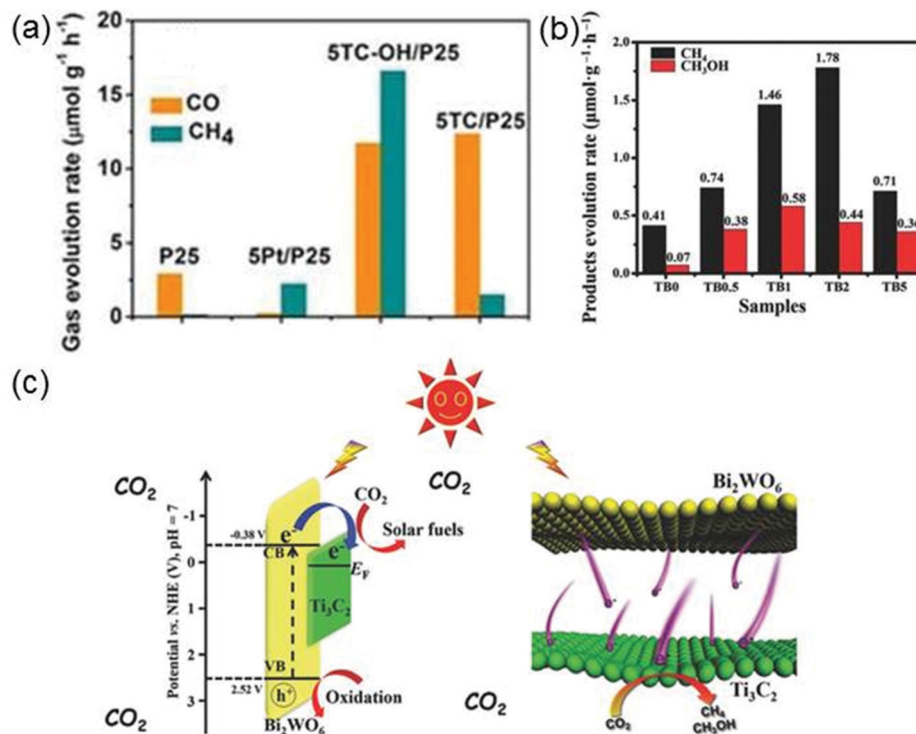
**Fig. 12** (a) Evolution rates of CO and $CH_4$ over P25, 5Pt/P25 (containing 5 wt% Pt), $5Ti_3C_2T_x$/P25 (containing 5 wt% $Ti_3C_2T_x$) and 5TCOH/P25 (containing 5 wt% $Ti_3C_2T_x$–OH) under the irradiation of a 300 W Xe lamp. Reprinted with permission from ref. 36 Copyright (2018) Wiley Online Library. (b) Photocatalytic activity (products evolution rates) of $Ti_3C_2T_x$–$Bi_2WO_6$ (TB) with different weights of $Ti_3C_2T_x$ (0, 0.5, 1, 2 and 5 wt%). (c) Energy level structure of the TB hybrid (left panel) and the photo-induced electron transfer process at the TB interface (right panel). Reprinted with permission from ref. 158 Copyright (2018) Advanced Science News.

and $Ti_3C_2T_x$ works as the co-catalyst) which are found to have much higher $CO_2$ adsorption capability and more efficient interfacial charge transfer ability than isolated $Bi_2WO_6$.[158] The excellent performance of $Ti_3C_2T_x$–$Bi_2WO_6$ (TB) originates from its porous structure, large interface contact area and short-distance charge transport. Fig. 12b shows the evolution rates of products (methane ($CH_4$) and methanol ($CH_3OH$)) for different wt% (0–5 wt%) $Ti_3C_2T_x$-modified $Bi_2WO_6$ nanosheets used for photocatalytic $CO_2$ reduction. Among all considered samples, the TB2 where $Ti_3C_2T_x$ accounts for 2 wt% has the highest evolution rate for $CH_4$ and the second highest evolution rate for $CH_3OH$, which are 1.78 µmol $g^{-1}$ $h^{-1}$ and 0.44 µmol $g^{-1}$ $h^{-1}$, respectively. It is noted that the yield of $CH_4$ and $CH_3OH$ over TB2 is 4.6 times that over the isolated $Bi_2WO_6$. The photocatalytic mechanism of ultrathin TB is described in Fig. 12c. Under solar irradiation, photo-induced electrons are generated on $Bi_2WO_6$, then the electrons move through the ultrathin layered heterojunction to the $Ti_3C_2T_x$ surface and react with the adsorbed $CO_2$ molecules.

## 5.2 Water remediation

Water pollution is a severe ecological and environmental issue.[159] The contaminants include heavy metal ions, organic substances (dyes), eutrophic substances and nuclear waste. Various methods such as adsorption, biological treatment, chemical oxidation and catalytic degradation have been developed for

wastewater treatment. Among those methods, adsorption and catalytic degradation are ideal methods for removing harmful substances from water. Owing to their advantages of easy preparation, large specific surface area and good reducibility, MXenes, as new adsorbents, are expected to play an important role in water remediation.

Considering that Ti has a high adsorption capacity for heavy metal ions, Ti-containing substances are considered as promising candidates to remove heavy metal ions from water.[160] By chemical exfoliation and alkalization treatment, Peng *et al.* have prepared hydroxyl-terminated $Ti_3C_2T_x$ (alk-$Ti_3C_2T_x$) which presents efficient lead ion (Pb(II)) uptake performance.[37] The purpose of alkalization is to form more hydroxyl groups on the surface of $Ti_3C_2T_x$, which will contribute to the adsorption of Pb(II). Significantly, each kilogram (kg) of $Ti_3C_2T_x$ can treat 4500 kg water containing Pb(II), and the content of remanent Pb(II) in water can successfully reach the drinking water standard recommended by the WHO (10 µg $L^{-1}$). In the actual situation, there are various kinds of metal ions in wastewater, thus it is necessary to determine whether common metal ions (Ca and Mg cations) in wastewater affect the adsorption selectivity of alk-$Ti_3C_2T_x$ toward Pb(II). Fig. 13a and b demonstrate that alk-$Ti_3C_2T_x$ still exhibits a distinctly selective adsorption for Pb(II) in a solution containing Ca(II) or Mg(II). By increasing the ratio of Ca(II)/Pb(II) (or Ca(II)/Mg(II)) in the solution, the selectivity of the alk-$Ti_3C_2T_x$ to Pb(II) can exceed that of the
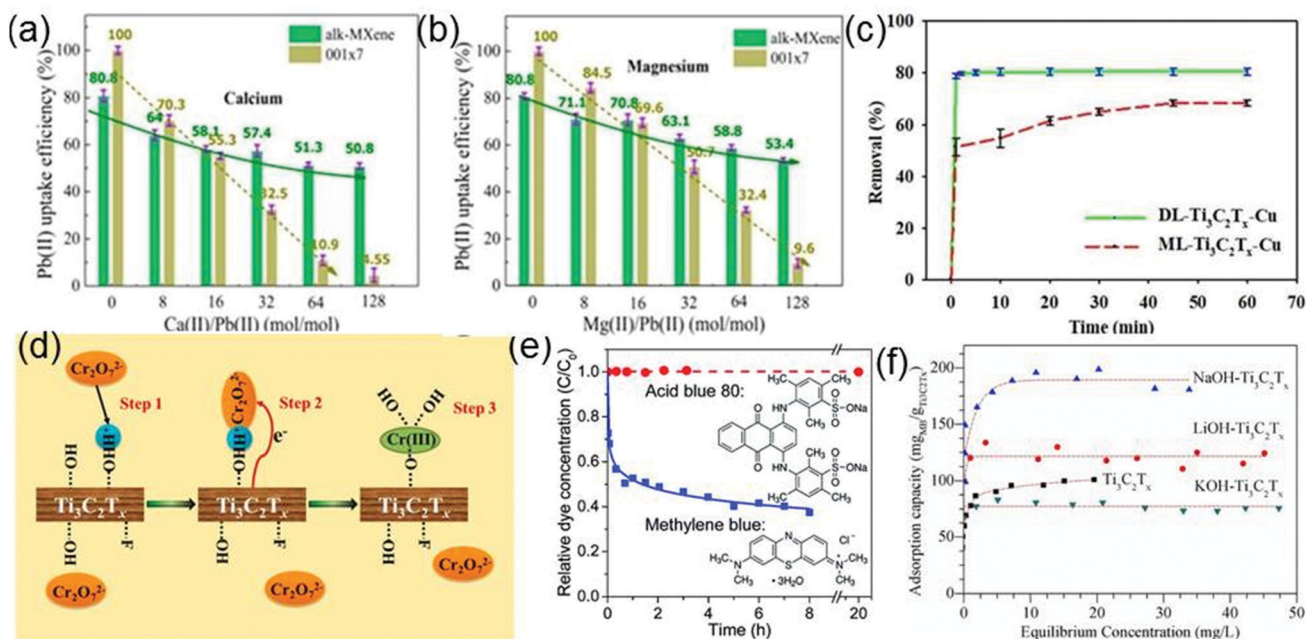
**Fig. 13** Effects of the coexisting calcium (a) or magnesium (b) ions in water on the selective adsorption of lead ions onto alk-$Ti_3C_2T_x$ and 001×7. Reprinted with permission from ref. 37 Copyright (2014) American Chemical Society. (c) Comparison of Cu ion removal by DL-$Ti_3C_2T_x$ and by ML-$Ti_3C_2T_x$. Reprinted with permission from ref. 163 Copyright (2017) American Chemical Society. (d) Schematic diagrams of the mechanism responsible for Cr(VI) removal by the $Ti_3C_2T_x$ nanosheets. Reprinted with permission from ref. 161 Copyright (2015) American Chemical Society. (e) Evolutions of concentrations of MB and AB80 in aqueous solutions containing suspended $Ti_3C_2T_x$ particles as a function of time in the dark. Reproduced with permission from ref. 38 Copyright (2014) Royal Society of Chemistry. (f) Adsorption isotherms of MB on $Ti_3C_2T_x$, LiOH−$Ti_3C_2T$ and NaOH−$Ti_3C_2T_x$ and KOH−$Ti_3C_2T_x$. Reprinted with permission from ref. 164 Copyright (2017) Elsevier.

traditional adsorbent 001×7. It is noticed that the Pb(II) adsorption is a pH-dependent process ($Ti_3C_2T_x$ exhibits the best Pb(II) sorption performance after the pH value is changed from 5 to 7) and the used $Ti_3C_2T_x$ can be regenerated by acidic solutions.

As a kind of heavy metal ion that widely exists in industrial wastewater, Cr(VI) is highly toxic to plants, animals, and the human body.[161] Hence, the industrial wastewater must undergo Cr(VI) adsorption treatment. Since $Ti_3C_2T_x$ has been successfully used for the adsorption of heavy metal Pb ions, it is expected that $Ti_3C_2T_x$ also has the potential for removing Cr(VI) from wastewater. Ying et al. find that the $Ti_3C_2T_x$ indeed shows an outstanding removal capacity for Cr(VI) as large as 250 mg g$^{-1}$. After treatment by $Ti_3C_2T_x$, the residual Cr(VI) concentration in the water becomes lower than the standard concentration of Cr(VI) stipulated by the World Health Organization in drinking water.[162] As shown in Fig. 13d, the removal process of Cr(VI) can be mainly divided into three steps: (1) Cr(VI) is attracted to the surface of $Ti_3C_2T_x$ with abundant protonated hydroxyl groups and adhered on the surface; (2) the absorbed Cr(VI) is reduced to Cr(III) by $Ti_3C_2T_x$; (3) the produced Cr(III) form Ti–O–Cr(III) links with the surface Ti–O bonds via covalent bonding. The Cr(VI) removal is also a pH-dependent process where the performance of $Ti_3C_2T_x$ towards the Cr(VI) removal is the best at the pH of 5.

Shahzad et al. confirm that $Ti_3C_2T_x$ nanosheets also have a strong adsorption capacity for Cu ions and delaminated (DL)-$Ti_3C_2T_x$ exhibits a more excellent adsorption capacity than multilayered-$Ti_3C_2T_x$ (Fig. 13c).[163] The highest adsorption

capacity of DL-$Ti_3C_2T_x$ toward Cu ions is 78.45 mg g$^{-1}$, which is 1.17 and 2.7 times those of the multilayered-$Ti_3C_2T_x$ and commonly used activated carbon, respectively. The adsorption mechanism is uncovered by the XRD analysis of DL-$Ti_3C_2T_x$. After the adsorption of Cu ions, the XRD pattern shows the emergence of the precipitates $Cu_2O$ and CuO, suggesting that Cu ions react with the surface functional groups of DL-$Ti_3C_2T_x$, generating $Cu_2O$ and CuO. To present the actual adsorption capacity of DL-$Ti_3C_2T_x$ for Cu ions, it is immersed in the simulated electroplating wastewater containing four kinds of heavy metal ions ($Cu^{2+}$, $Pb^{2+}$, $Cd^{2+}$, and $Cr^{3+}$). After 5 hours, the removal efficiencies of four metal ions are 98.29%, 90.04%, 52.90%, and 73.64%, respectively, which demonstrates that the $Cu^{2+}$ adsorption capacity of DL-$Ti_3C_2T_x$ is not affected by common cations in wastewater. The above result also shows the potential of $Ti_3C_2T_x$ for treating multiple heavy metal ions in water.

As potential adsorbents, MXenes are also applied to dye sewage treatment. Mashtalir et al. investigate the adsorption capacity of $Ti_3C_2T_x$ for AB80 (an anionic dye) and MB (a cationic dye).[38] Fig. 13e shows the time dependence of the removal of AB80 and MB from solution in the dark by $Ti_3C_2T_x$. After 20 h, the concentration of AB80 has no change, but the MB concentration displays a dramatic decrease within 8 h. Apparently, $Ti_3C_2T_x$ preferentially captures the cationic dye, which is closely related to the negatively charged surface of $Ti_3C_2T_x$ that can bind strongly with MB.

In order to enhance the dye adsorption capacity and the stability of $Ti_3C_2T_x$ in water, Wei et al. adjust the surface

functional groups and the internal structure of $Ti_3C_2T_x$ by alkalization.[164] Experimentally, they use three alkaline solutions (LiOH, NaOH and KOH) respectively to treat $Ti_3C_2T_x$ and obtain $LiOH–Ti_3C_2T_x$, $NaOH–Ti_3C_2T_x$ and $KOH–Ti_3C_2T_x$ which have distinctly different adsorption isotherms for MB (Fig. 13f). In particular, the MB adsorption capacity of $NaOH–Ti_3C_2T_x$ reaches 189 mg g$^{-1}$, which is substantially higher than those of pristine $Ti_3C_2T_x$, $LiOH–Ti_3C_2T_x$ and $KOH–Ti_3C_2T_x$. During the adsorption process, the MB molecules intercalate into alkalized $Ti_3C_2T_x$, leading to the increase of the adsorption capacity of $Ti_3C_2T_x$. $NaOH–Ti_3C_2T_x$ has more stacking gaps than $LiOH–Ti_3C_2T_x$ and $KOH–Ti_3C_2T_x$, which provides more positions for the MB intercalation adsorption.

In addition to heavy metal ions and dyes, MXenes and their composites can also treat eutrophic substances in wastewater. The synthesis of a sandwich-like $Ti_3C_2T_x/Fe_3O_4/Fe_2O_3$ nanocomposite (MXI) makes it possible to use MXenes for water eutrophication (phosphate) remediation. In the MXI, the nano-$Fe_2O_3$ is distributed in the interior layers of the MXenes and increases the number of available activated Ti–OH layers, and $Fe_3O_4$ inserts into the gaps between the multiple layers of MXene, forming the Fe–OH species that facilitate the preferential adsorption of phosphate and improve the sorption capability.[165] In practical application, each kilogram of MXI can handle 2300/2400 kilograms of phosphorus-containing wastewater, indicating that MXI can be used for wastewater treatment on a large scale. Moreover, the used $Ti_3C_2T_x/Fe_3O_4/Fe_2O_3$ can be regenerated repeatedly by soaking the sample in the mixture solution of alkaline and salt.

With increasing utilization of nuclear energy, nuclear waste is becoming a worldwide environmental problem. To remedy nuclear contamination, the adsorption technique is widely used for the removal and separation of radionuclides. Therefore, the development of effective adsorbents for nuclear waste is very important. MXenes with a large surface area and abundant active sites are considered as ideal adsorbents for nuclear waste. In the MXene family, $Ti_3C_2(OH)_2$ is firstly studied as a promising adsorbent for the hydrated uranyl cation $[UO_2(H_2O)_5]^{2+}$ by using density functional theory (DFT).[166] Soon afterwards, Wang et al. experimentally report that $V_2CT_x$ has a strong adsorption performance for uranium ions (U(VI)).[167] The adsorption capacity of $V_2CT_x$ can be up to 174 mg g$^{-1}$ which is even larger than that of the conventional inorganic nanomaterials. Moreover, they show that $V_2CT_x$ is the most stable at the pH of 5 and uranium-adsorbed $V_2CT_x$ can be reused after soaking in acidic solution (pH < 3). These above findings suggest the great promise of MXenes for applications in nuclear waste treatment.

In addition, researchers have also explored the antibacterial properties of MXenes for their potential use as biocides in water treatment.[168,169] As a representative material in the MXene family, $Ti_3C_2T_x$ has been verified by Rassol et al. to have a higher antibacterial efficiency toward both *Bacillus subtilis* (*B. subtilis*) and *Escherichia coli* (*E. coli*), compared with graphene oxide (GO)[168,169] that is widely reported as an antibacterial agent, which opens a door for MXenes' applications in antimicrobial coatings and water purification membranes. The excellent antibacterial activity of MXenes should be related to their hydrophilicity surfaces which may promote the inactivation of bacteria via direct contact interactions. The high-density defects and the functional groups on MXenes could also strengthen the antibacterial activity. In the bactericidal process, a variety of chemical reactions of MXenes with bacterial membranes are possible, however, they need further investigations.

## 5.3 Sensor

Due to their large specific surface area, excellent conductive properties, and good biocompatibility, 2D materials have been used in sensors for more than ten years.[170–179] Not surprisingly, MXenes have exhibited excellent performances in biosensors and gas sensors.

In a biosensor, the active protein usually loses its bioactivity when it directly contacts the electrode surface, hence specific materials are selected to immobilize active proteins and maintain their activity. Notably, MXenes, as protein immobilization matrixes, can not only help to protect active proteins but also facilitate the direct electron transfer between the enzyme and the electrode, yielding a possibility of fabricating mediator-free biosensors.

$Ti_3C_2T_x$ has firstly been chosen to immobilize hemoglobin (Hb) in the biosensor (Nafion/Hb/$Ti_3C_2T_x$/GCE) for detecting nitrites.[180] Because of the relatively high conductivity of $Ti_3C_2T_x$, the Nafion/Hb/$Ti_3C_2T_x$/GCE biosensor shows an excellent biosensor performance with an enlarged detection range and a reduced detection limit. Specifically speaking, the nitrite detection range of the biosensor reaches 0.5–11 800 μM and the lowest detection limit is lowered to 0.12 μM.

Recently, it is found that a $TiO_2$-modified $Ti_3C_2T_x$ nanocomposite synthesized by a hydrothermal process can also be used as the immobilization matrix for hemoglobin in the biosensor (Nafion/Hb/$Ti_3C_2T_x$–$TiO_2$/GCE) detecting hydrogen peroxide.[40] The microstructure of this nanocomposite is shown in Fig. 14a where one can see that the $Ti_3C_2T_x$ nano-layers exhibit an organ-like structure with one end closing and the other end opening, and numerous white $TiO_2$ nanoparticles are loaded on the $Ti_3C_2T_x$ layers. The organ-like structure is beneficial to the enzyme immobilization on the inner surfaces of $Ti_3C_2T_x$. Moreover, $TiO_2$ possesses excellent biocompatibility and chemical stability, which can provide a protective microenvironment for the enzymes. Fig. 14b displays the schematic illustration for the $TiO_2$–$Ti_3C_2T_x$ nanocomposite encapsulating hemoglobin. The enzyme is immobilized on the inner surfaces of the organ-like structured $Ti_3C_2T_x$ nano-layers and adjacent to $TiO_2$, which ensures the stability and activity of the enzyme for a long time. Compared with the biosensor Nafion/Hb/$Ti_3C_2T_x$/GCE where $Ti_3C_2T_x$ acts as the immobilization matrix, the Nafion/Hb/$TiO_2$–$Ti_3C_2T_x$/GCE biosensor has a faster response (a response time of less than 3 s) and a wider linear range from 0.1 to 380 μM.

In the biosensor for glucose detection, Au nanostructures are widely used to retain the biological activity of enzymes and reduce the insulating effect of the protein shell for direct electron transfer.[181–187] In order to make MXene have an
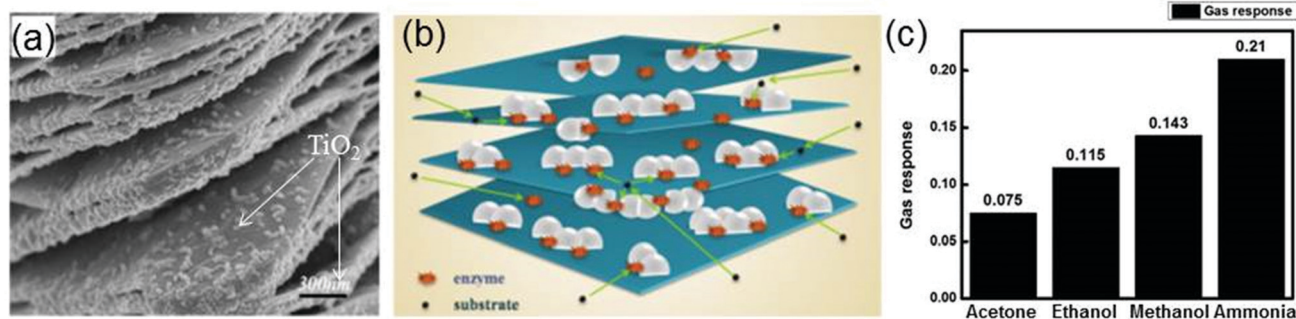
Fig. 14 (a) SEM image of the $TiO_2-Ti_3C_2$ nanocomposite. (b) Schematic illustration of the $TiO_2-Ti_3C_2$ nanocomposite. Reprinted with permission from ref. 40 Copyright (2015) Elsevier. (c) Response of the $Ti_3C_2T_x$ sensor to four different gases. Reprinted with permission from ref. 191 Copyright (2017) American Chemical Society.

excellent performance in the enzymatic glucose biosensor, a MXene–Au nanocomposite with a structure similar to that of $TiO_2-Ti_3C_2T_x$ mentioned above is used as the immobilization matrix in a GOx/Au/MXene/Nafion/GC biosensor.[188] It is amazing that the fabricated biosensor shows a wide detection range for the glucose concentration from 0.1 mM to 18 mM, a low detection limit of 5.9 μM, excellent stability and good reproducibility. The Au nanoparticles distributed on the surfaces of MXene nanosheets further improve the electrical conductivity of MXene, which will strongly promote the electron exchange between the active center of enzymes and the electrode.

MXenes can be used in not only biosensors but also gas sensors.[189–191] The utilization of MXenes in gas sensors overcomes conventional gas sensors' drawback of a lack of selectivity for particular gas $NH_3$. Based on first-principles calculations, Yu et al. firstly investigate the adsorption of gas molecules ($NH_3$, $H_2$, $CH_4$, CO, $CO_2$, $N_2$, $NO_2$, and $O_2$) on monolayer $Ti_2CO_2$.[41] It is found that $NH_3$ is preferentially adsorbed on $Ti_2CO_2$, compared with other molecules. After $NH_3$ adsorption, the calculated current–voltage relation curve of $Ti_2CO_2$ shows a large fluctuation, in contrast to the weak fluctuations of the corresponding curves of $MoS_2$ and phosphorene in the same case, indicating the high sensitivity of $Ti_2CO_2$ to $NH_3$.[41] Inspired by this theoretical study, the gas sensor based on MXenes–$Ti_3C_2T_x$ is fabricated subsequently. It is found that this sensor can successfully measure various gases (ethanol, methanol, acetone, and $NH_3$) at room temperature and shows p-type sensing behavior. The average gas responses of $Ti_3C_2T_x$ for ethanol, methanol, acetone, and ammonia are shown in Fig. 14c. Obviously, the $Ti_3C_2T_x$ sensor shows the highest response to $NH_3$ and the lowest response to acetone. The sensing mechanism of the $Ti_3C_2T_x$ sensor involves absorption/desorption of gases by both defects and functional groups of $Ti_3C_2T_x$.[191]

# 6 Conclusions and outlook

This review summarizes recent progress of MXenes and MXene-based composites in their synthesis, properties and applications. More than 20 different MXenes have been produced in the past few years by selectively etching and exfoliation of layered ternary metal carbides, nitrides or carbonitrides. This synthetic process leads to the surface decorations of MXenes by various functional groups including O, F and OH, where the proportions of different functional groups are arbitrary, depending on the etching time and temperature. Due to this versatile surface chemistry, MXenes have exhibited many fascinating electronic, magnetic, electrochemical and mechanical properties. Several novel quantum phenomena including half-metallicity and topological insulativity are also predicted for some MXenes, which is appealing for 2D spintronics. Thanks to their excellent flexibility, 2D morphology and layered structures, MXenes easily form multifarious composites with other materials, which offers an effective way to tune the properties and performances of MXenes for various applications. For example, using metal oxides and CNTs as fillers in MXenes can not only improve the specific capacity of MXenes but also provide additional electron conductive pathways and promote electrolyte ion transportation, which will lead to the great enhancement of the overall electrochemical performances of MXenes.

Due to the unique morphologies, layered structures and excellent properties, MXenes and their composites have good application prospects in catalysis, water remediation and sensors. As catalysts or co-catalysts, MXenes and their composites are widely used in electro/photocatalytic water splitting and photocatalytic reduction of $CO_2$, where the excellent performances of certain MXene and MXene-based materials suggest that they have great potential to replace traditional precious metal catalysts. In sewage treatment, large surface areas and specific surface groups have endowed $Ti_3C_2T_x$ and its composites with strong adsorption abilities for heavy metal ions, dyes and eutrophic substances, enabling that they can be used as adsorbents for water remediation. Additionally, MXenes and their composites with high conductivity and good biocompatibility can immobilize enzyme and facilitate the direct electron transfer between the enzyme and the electrode in various biosensors. It is also amazing to find that some MXenes, e.g., $Ti_3C_2T_x$, are sensitive to $NH_3$ and can convert the $NH_3$ concentration into electrical signals, making it possible to fabricate MXene-based $NH_3$ sensors which will overcome conventional gas sensors' drawback of a lack of selectivity for $NH_3$.

Note that compared with graphene, MXenes' study is still at an early stage. Opportunities and challenges coexist in the future research of MXenes. In the aspect of synthesis, (i) many MXenes such as $Sc_2C$, $Hf_2C$, $W_2C$ and so on are predicted to be able to stably exist, but their precursors have not yet been produced. Therefore, the synthesis of new MAX phases or other layered carbide and nitride precursors will be of significance for expanding the MXene family. (ii) It is highly desirable to develop new methods for synthesizing high-quality MXenes with large lateral dimensions, fewer defects and controlled surface terminations. In particular, achieving uniform terminations with only a single type of functional group is the most challenging task for experimentalists. Ultimately, bare MXenes without surface terminations must be synthesized, by chemical vapor deposition (CVD) or physical methods. In the aspect of property exploration, most of the known properties are predicted by theoretical calculations and await experimental verification. Particularly, semiconductivity has not been observed in MXenes, in spite of theoretical predictions. Moreover, there have been no reports on experimental measurements of the band structures of MXenes which are important to understand the fundamental properties of MXenes. It is also necessary to understand the structures and properties of MXenes intercalated with various ions or compounds. In the aspect of applications, although MXenes have shown excellent performances in many application fields, many underlying physical mechanisms still need to be intensively explored. For example, a deep understanding of catalytic and electrocatalytic properties of various MXene-based composites is essential for designing new high-efficient catalysts and may open new avenues in clean-energy conversion. Moreover, the mechanism for the high sensitivity of MXenes to $NH_3$ remains elusive, which limits the practical applications of MXene-based gas sensors.

Finally, it is highly recommended to combine experimental and computational studies in the future explorations of MXenes. Considering different surface terminations and elemental compositions, there are hundreds of MXene members. The prior computational predictions of the properties and application potentials of MXenes could guide experimentalists to synthesize and investigate the most promising compounds, which will greatly reduce the research cost. Recently, it has been shown that machine learning can accurately predict the band gaps of MXenes.[192] It is reasonable to expect that machine learning will play a significant role in predicting the properties of MXenes in the foreseeable future.

## Conflicts of interest

There are no conflicts to declare.

## Acknowledgements

## References

1 Y. Shao, J. Wang, H. Wu, J. Liu, I. A. Aksay and Y. Lin, *Electroanalysis*, 2010, **22**, 1027–1036.

2 M. J. Allen, V. C. Tung and R. B. Kaner, *Chem. Rev.*, 2009, **110**, 132.

3 C. Mattevi, H. Kim and M. Chhowalla, *J. Mater. Chem.*, 2011, **21**, 3324–3334.

4 H. Wang, T. Maiyalagan and X. Wang, *ACS Catal.*, 2012, **2**, 781–794.

5 L. Li, Y. Yu, G. J. Ye, Q. Ge, X. Ou, H. Wu, D. Feng, X. H. Chen and Y. Zhang, *Nat. Nanotechnol.*, 2014, **9**, 372–377.

6 B. Lalmi, H. Oughaddou, H. Enriquez, A. Kara, S. Vizzini, B. Ealet and B. Aufray, *Appl. Phys. Lett.*, 2010, **97**, 223109.

7 M. E. Dávila, L. Xian, S. Cahangirov, A. Rubio and G. Le Lay, *New J. Phys.*, 2014, **16**, 095002.

8 H. Liu, A. T. Neal, Z. Zhu, Z. Luo, X. Xu, D. Tománek and P. D. Ye, *ACS Nano*, 2014, **8**, 4033–4041.

9 S. Cahangirov, M. Topsakal, E. Aktürk, H. Şahin and S. Ciraci, *Phys. Rev. Lett.*, 2009, **102**, 236804.

10 G. R. Bhimanapati, Z. Lin, V. Meunier, Y. Jung, J. Cha, S. Das, D. Xiao, Y. Son, M. S. Strano, V. R. Cooper and L. Liang, *ACS Nano*, 2015, **9**, 11509–11539.

11 X. Tang, X. Guo, W. Wu and G. Wang, *Adv. Energy Mater.*, 2018, **8**, 1801897.

12 B. Anasori, M. R. Lukatskaya and Y. Gogotsi, *Nat. Rev. Mater.*, 2017, **2**, 16098.

13 M. Naguib, V. N. Mochalin, M. W. Barsoum and Y. Gogotsi, *Adv. Mater.*, 2014, **26**, 992–1005.

14 K. Hantanasirisakul and Y. Gogotsi, *Adv. Mater.*, 2018, **30**, e1804779.

15 M. Khazaei, A. Ranjbar, M. Arai, T. Sasaki and S. Yunoki, *J. Mater. Chem. C*, 2017, **5**, 2488–2503.

16 Y. T. Liu, X. D. Zhu and L. Pan, *Small*, 2018, **14**, e1803632.

17 J. Nan, X. Guo, J. Xiao, X. Li, W. Chen, W. Wu, H. Liu, Y. Wang, M. Wu and G. Wang, *Small*, 2019, e1902085.

18 V. M. H. Ng, H. Huang, K. Zhou, P. S. Lee, W. Que, J. Z. Xu and L. B. Kong, *J. Mater. Chem. A*, 2017, **5**, 3039–3068.

19 M. W. Barsoum and T. El-Raghy, *Am. Sci.*, 2001, **89**, 334–343.

20 M. W. Barsoum, *Prog. Solid State Chem.*, 2000, **28**, 201–281.

21 Z. M. Sun, *Int. Mater. Rev.*, 2013, **56**, 143–166.

22 H. Högberg, L. Hultman, J. Emmerlich, T. Joelsson, P. Eklund, J. M. Molina-Aldareguia, J.-P. Palmquistc and U. Wilhelmsson, *Surf. Coat. Technol.*, 2005, **193**, 6–10.

23 X. Zhang, J. Xu, H. Wang, J. Zhang, H. Yan, B. Pan, J. Zhou and Y. Xie, *Angew. Chem., Int. Ed.*, 2013, **52**, 4361–4365.

24 M. Naguib, M. Kurtoglu, V. Presser, J. Lu, J. Niu, M. Heon, L. Hultman, Y. Gogotsi and M. W. Barsoum, *Adv. Mater.*, 2011, **23**, 4248–4253.

25 G. R. Berdiyorov and K. A. Mahmoud, *Appl. Surf. Sci.*, 2017, **416**, 725–730.

26  S. Li, P. Tuo, J. Xie, X. Zhang, J. Xu, J. Bao, B. Pan and Y. Xie, *Nano Energy*, 2018, **47**, 512–518.

27  X. Liang, A. Garsuch and L. F. Nazar, *Angew. Chem., Int. Ed.*, 2015, **54**, 3907–3911.

28  X. Liang, Y. Rangom, C. Y. Kwok, Q. Pang and L. F. Nazar, *Adv. Mater.*, 2017, **29**, 1603040.

29  O. Mashtalir, M. R. Lukatskaya, M. Q. Zhao, M. W. Barsoum and Y. Gogotsi, *Adv. Mater.*, 2015, **27**, 3501–3506.

30  Y. Xie, M. Naguib, V. N. Mochalin, M. W. Barsoum, Y. Gogotsi, X. Yu, K. W. Nam, X. Q. Yang, A. I. Kolesnikov and P. R. Kent, *J. Am. Chem. Soc.*, 2014, **136**, 6385–6394.

31  X. Wang, S. Kajiyama, H. Iinuma, E. Hosono, S. Oro, I. Moriguchi, M. Okubo and A. Yamada, *Nat. Commun.*, 2015, **6**, 6544.

32  X. Xie, M. Q. Zhao, B. Anasori, K. Maleski, C. E. Ren, J. Li, B. W. Byles, E. Pomerantseva, G. Wang and Y. Gogotsi, *Nano Energy*, 2016, **26**, 513–523.

33  J. Yan, C. E. Ren, K. Maleski, C. B. Hatter, B. Anasori, P. Urbankowski, A. Sarycheva and Y. Gogotsi, *Adv. Funct. Mater.*, 2017, **27**, 1701264.

34  Y. Cheng, Y. Zhang, Y. Li, J. Dai and Y. Song, *J. Mater. Chem. A*, 2019, **7**, 9324–9334.

35  Z. Guo, J. Zhou, L. Zhu and Z. Sun, *J. Mater. Chem. A*, 2016, **4**, 11446–11452.

36  M. Ye, X. Wang, E. Liu, J. Ye and D. Wang, *ChemSusChem*, 2018, **11**, 1606–1611.

37  Q. Peng, J. Guo, Q. Zhang, J. Xiang, B. Liu, A. Zhou, R. Liu and Y. Tian, *J. Am. Chem. Soc.*, 2014, **136**, 4113–4116.

38  O. Mashtalir, K. M. Cook, V. N. Mochalin, M. Crowe, M. W. Barsoum and Y. Gogotsi, *J. Mater. Chem. A*, 2014, **2**, 14334–14338.

39  Q. Zhang, J. Teng, G. Zou, Q. Peng, Q. Du, T. Jiao and J. Xiang, *Nanoscale*, 2016, **8**, 7085–7093.

40  F. Wang, C. Yang, M. Duan, Y. Tang and J. Zhu, *Biosens. Bioelectron.*, 2015, **74**, 1022–1028.

41  X. F. Yu, Y. C. Li, J. B. Cheng, Z. B. Liu, Q. Z. Li, W. Z. Li, X. Yang and B. Xiao, *ACS Appl. Mater. Interfaces*, 2015, **7**, 13707–13713.

42  X. H. Wang and Y. C. Zhou, *J. Mater. Sci. Technol.*, 2010, **26**, 385–416.

43  K. Zhu, Y. Jin, F. Du, S. Gao, Z. Gao, X. Meng, G. Chen, Y. Wei and Y. Gao, *J. Mater. Chem.*, 2018, **31**, 1–8.

44  M. Naguib, J. Halim, J. Lu, K. M. Cook, L. Hultman, Y. Gogotsi and M. W. Barsoum, *J. Am. Chem. Soc.*, 2013, **135**, 15966–15969.

45  A. VahidMohammadi, A. Hadjikhani, S. Shahbazmohamadi and M. Beidaghi, *ACS Nano*, 2017, **11**, 11135–11144.

46  B. Soundiraraju and B. K. George, *ACS Nano*, 2017, **11**, 8892–8900.

47  M. Naguib, O. Mashtalir, J. Carle, V. Presser, J. Lu, L. Hultman, Y. Gogotsi and M. W. Barsoum, *ACS Nano*, 2012, **6**, 1322–1331.

48  Q. Tao, M. Dahlqvist, J. Lu, S. Kota, R. Meshkian, J. Halim, J. Palisaitis, L. Hultman, M. W. Barsoum, P. O. A. Persson and J. Rosen, *Nat. Commun.*, 2017, **8**, 14949.

49  J. Halim, J. Palisaitis, J. Lu, J. Thörnberg, E. J. Moon, M. Precner, P. Eklund, P. O. Å. Persson, M. W. Barsoum and J. Rosen, *ACS Appl. Nano Mater.*, 2018, **1**, 2455–2460.

50  R. Meshkian, M. Dahlqvist, J. Lu, B. Wickman, J. Halim, J. Thornberg, Q. Tao, S. Li, S. Intikhab, J. Snyder, M. W. Barsoum, M. Yildizhan, J. Palisaitis, L. Hultman, P. O. A. Persson and J. Rosen, *Adv. Mater.*, 2018, **30**, e1706409.

51  X. Wang, X. Shen, Y. Gao, Z. Wang, R. Yu and L. Chen, *J. Am. Chem. Soc.*, 2015, **137**, 2715–2721.

52  H. W. Wang, M. Naguib, K. Page, D. J. Wesolowski and Y. Gogotsi, *J. Am. Chem. Soc.*, 2016, **28**, 349–359.

53  S. Zhao, X. Menga, K. Zhu, F. Du, G. Chen, Y. Wei, Y. Gogotsi and Y. Gao, *Energy Storage Mater.*, 2017, **8**, 42–48.

54  M. H. Tran, T. Schäfer, A. Shahraei, M. Dürrschnabel, L. Molina-Luna, U. I. Kramm and C. S. Birkel, *ACS Appl. Energy Mater.*, 2018, **1**, 3908–3914.

55  B. Anasori, Y. Xie, M. Beidaghi, J. Lu and M. W. Barsoum, *ACS Nano*, 2015, **9**, 9507–9516.

56  M. Ghidiu, M. R. Lukatskaya, M. Q. Zhao, Y. Gogotsi and M. W. Barsoum, *Nature*, 2014, **516**, 78–81.

57  S. Kajiyama, L. Szabova, H. Iinuma, A. Sugahara, K. Gotoh, K. Sodeyama, Y. Tateyama, M. Okubo and A. Yamada, *Adv. Sci. News*, 2016, **7**, 1601873.

58  J. Halim, S. Kota, M. R. Lukatskaya, M. Naguib, M. Q. Zhao, E. J. Moon, J. Pitock, J. Nanda, S. J. May, Y. Gogotsi and M. W. Barsoum, *Adv. Funct. Mater.*, 2016, **26**, 3118–3127.

59  F. Liu, J. Zhou, S. Wang, B. Wang, C. Shen, L. Wang, Q. Hu, Q. Huang and A. Zhou, *J. Electrochem. Soc.*, 2017, **164**, A709–A713.

60  F. Du, H. Tang, L. Pan, T. Zhang, H. Lu, J. Xiong, J. Yang and C. J. Zhang, *Electrochim. Acta*, 2017, **235**, 690–699.

61  B. Anasori, Y. Xie, M. Beidaghi, J. Lu, B. C. Hosler, L. Hultman, P. R. C. Kent, Y. Gogotsi and M. W. Barsoum, *ACS Nano*, 2015, **9**, 9507–9516.

62  J. Yang, M. Naguib, M. Ghidiu, L.-M. Pan, J. Gu, J. Nanda, J. Halim, Y. Gogotsi and M. W. Barsoum, *J. Am. Ceram. Soc.*, 2015, **99**, 660–666.

63  J. Halim, M. R. Lukatskaya, K. M. Cook, J. Lu, C. R. Smith, L. A. Naslund, S. J. May, L. Hultman, Y. Gogotsi, P. Eklund and M. W. Barsoum, *Chem. Mater.*, 2014, **26**, 2374–2381.

64  A. Feng, Y. Yu, F. Jiang, Y. Wang, L. Mi, Y. Yu and L. Song, *Ceram. Int.*, 2017, **43**, 6322–6328.

65  L. Wang, H. Zhang, B. Wang, C. Shen, C. Zhang, Q. Hu, A. Zhou and B. Liu, *Electron. Mater. Lett.*, 2016, **12**, 702–710.

66  P. Urbankowski, B. Anasori, T. Makaryan, D. Er, S. Kota, P. L. Walsh, M. Zhao, V. B. Shenoy, M. W. Barsoum and Y. Gogotsi, *Nanoscale*, 2016, **8**, 11385–11391.

67  Y. C. Zhou, L. F. He, Z. J. Lin and J. Y. Wang, *J. Eur. Ceram. Soc.*, 2013, **33**, 2831–2865.

68  J. Zhou, X. Zha, F. Y. Chen, Q. Ye, P. Eklund, S. Du and Q. Huang, *Angew. Chem., Int. Ed.*, 2016, **55**, 5008–5013.

69  J. Zhou, X. Zha, X. Zhou, F. Chen, G. Gao, S. Wang, C. Shen, T. Chen, C. Zhi, P. Eklund, S. Du, J. Xue, W. Shi, Z. Chai and Q. Huang, *ACS Nano*, 2017, **11**, 3841–3850.

70  R. Meshkian, L.-Å. Näslund, J. Halim, J. Lu, M. W. Barsoum and J. J. S. M. Rosen, *Scr. Mater.*, 2015, **108**, 147–150.

71  O. Mashtalir, M. Naguib, V. N. Mochalin, Y. Dall'Agnese, M. Heon, M. W. Barsoum and Y. Gogotsi, *Nat. Commun.*, 2013, **4**, 1716.

72  Y. Wu, P. Nie, J. Wang, H. Dou and X. Zhang, *ACS Appl. Mater. Interfaces*, 2017, **9**, 39610–39617.

73  C. E. Ren, K. B. Hatzell, M. Alhabeb, Z. Ling, K. A. Mahmoud and Y. Gogotsi, *J. Phys. Chem. Lett.*, 2015, **6**, 4026–4031.

74  H. Wang, J. Zhang, Y. Wu, H. Huang, G. Li, X. Zhang and Z. Wang, *Appl. Surf. Sci.*, 2016, **384**, 287–293.

75  M. Naguib, R. R. Unocic, B. L. Armstrong and J. Nanda, *Dalton Trans.*, 2015, **44**, 9353–9358.

76  T. Zhang, L. Pan, H. Tang, F. Du, Y. Guo, T. Qiu and J. Yang, *J. Alloys Compd.*, 2016, **695**, 818–826.

77  A. Lipatov, M. Alhabeb, M. R. Lukatskaya, A. Boson, Y. Gogotsi and A. Sinitskii, *Adv. Electron. Mater.*, 2016, **2**, 1600255.

78  Z. Ling, C. E. Ren, M. Q. Zhao, J. Yang, J. M. Giammarco, J. Qiu, M. W. Barsoum and Y. Gogotsi, *Proc. Natl. Acad. Sci. U. S. A.*, 2014, **111**, 16676–16681.

79  M. Naguib, T. Saito, S. Lai, M. S. Rager, T. Aytug, M. P. Paranthaman, M. Q. Zhao and Y. Gogotsi, *RSC Adv.*, 2016, **6**, 72069–72073.

80  H. Zhang, L. Wang, Q. Chen, P. Li, A. Zhou, X. Cao and Q. Hu, *Mater. Des.*, 2015, **92**, 682–689.

81  E. A. Mayerberger, O. Urbanek, R. M. McDaniel, R. M. Street, M. W. Barsoum and C. L. Schauer, *J. Appl. Polym. Sci.*, 2017, **134**, 45295.

82  J. Luo, X. Tao, J. Zhang, Y. Xia, H. Huang, L. Zhang, Y. Gan, C. Liang and W. Zhang, *ACS Nano*, 2016, **10**, 2491–2499.

83  J. Zhu, Y. Tang, C. Yang, F. Wang and M. Cao, *J. Electrochem. Soc.*, 2016, **163**, A785–A791.

84  C. Zhang, S. J. Kim, M. Ghidiu, M. Q. Zhao, M. W. Barsoum, V. Nicolosi and Y. Gogotsi, *Adv. Funct. Mater.*, 2016, **26**, 4143–4151.

85  J. Wang, S. Dong, H. Li, Z. Chen, S. Jiang, L. Wu and X. Zhang, *J. Electroanal. Chem.*, 2017, **810**, 27–33.

86  J. Huang, R. Meng, L. Zu, Z. Wang, N. Feng, Z. Yang, Y. Yu and J. Yang, *Nano Energy*, 2018, **46**, 20–28.

87  B. Ahmed, D. H. Anjum, Y. Gogotsi and H. N. Alshareef, *Electrochim. Acta*, 2017, **202**, 24–31.

88  M. Q. Zhao, M. Torelli, C. E. Ren, M. Ghidiu, Z. Ling, B. Anasori, M. W. Barsoum and Y. Gogotsi, *Nano Energy*, 2015, **30**, 603–613.

89  X. Guo, X. Xie, S. Choi, Y. Zhao, H. Liu, C. Wang, S. Chang and G. Wang, *J. Mater. Chem. A*, 2017, **5**, 12445–12452.

90  Y. Wang, Y. Li, Z. Qiu, X. Wu, P. Zhou, T. Zhou, J. Zhao, Z. Miao, J. Zhou and S. Zhuo, *J. Mater. Chem. A*, 2018, **6**, 11189–11197.

91  H. Zhang, H. Dong, X. Zhang, Y. Xu and J. Fransaer, *Electrochim. Acta*, 2016, **202**, 24–31.

92  M. Q. Zhao, C. E. Ren, Z. Ling, M. R. Lukatskaya, C. Zhang, K. L. Van Aken, M. W. Barsoum and Y. Gogotsi, *Adv. Mater.*, 2015, **27**, 339–345.

93  Y. Cai, J. Shen, G. Ge, Y. Zhang, W. Jin, W. Huang, J. Shao, J. Yang and X. Dong, *ACS Nano*, 2018, **12**, 56–62.

94  Y. Bai, K. Zhou, N. Srikanth, J. H. Pang, X. He and R. Wang, *RSC Adv.*, 2016, **6**, 35731–35739.

95  X. H. Zha, K. Luo, Q. Li, Q. Huang, J. He, X. Wen and S. Du, *EPL*, 2015, **111**, 26007.

96  Z. Guo, J. Zhou, C. Si and Z. Sun, *Phys. Chem. Chem. Phys.*, 2015, **17**, 15348–15354.

97  U. Yorulmaz, A. Özden, N. K. Perkgöz, F. Ay and C. Sevik, *Nanotechnology*, 2016, **27**, 335702.

98  V. N. Borysiuk, V. N. Mochalin and Y. Gogotsi, *Nanotechnology*, 2015, **26**, 265705.

99  M. Khazaei, M. Arai, T. Sasaki, A. Ranjbar, Y. Liang and S. Yunoki, *Phys. Rev. B: Condens. Matter Mater. Phys.*, 2015, **92**, 075411.

100  Y. Liu, H. Xiao and W. A. Goddard, *J. Am. Chem. Soc.*, 2016, **138**, 15853–15856.

101  J. Xu, J. Shim, J. H. Park and S. J. A. F. M. Lee, *Adv. Funct. Mater.*, 2016, **26**, 5328–5334.

102  Q. Peng, C. Si, J. Zhou and Z. Sun, *Appl. Surf. Sci.*, 2019, **480**, 199–204.

103  H. Wang, C. Si, J. Zhou and Z. Sun, *J. Phys. Chem. C*, 2017, **121**, 25164–25171.

104  Q. H. Wang, K. Kalantar-Zadeh, A. Kis, J. N. Coleman and M. S. Strano, *Nat. Nanotechnol.*, 2012, **7**, 699–712.

105  A. Allain, J. Kang, K. Banerjee and A. Kis, *Nat. Mater.*, 2015, **14**, 1195–1205.

106  J. You, C. Si, J. Zhou and Z. Sun, *J. Phys. Chem. C*, 2019, **123**, 3719–3726.

107  T. Hu, H. Zhang, J. Wang, Z. Li, M. Hu, J. Tan, P. Hou, F. Li and X. Wang, *Sci. Rep.*, 2015, **5**, 16329.

108  C. E. Ren, M. Q. Zhao, T. Makaryan, J. Halim, M. Boota, S. Kota, B. Anasori, M. W. Barsoum and Y. Gogotsi, *ChemElectroChem*, 2016, **3**, 689.

109  M.-Q. Zhao, M. Torelli, C. E. Ren, M. Ghidiu, Z. Ling, B. Anasori, M. W. Barsoum and Y. Gogotsi, *Nano Energy*, 2016, **30**, 603.

110  T. Zhang, L. Pan, H. Tang, F. Du, Y. Guo, T. Qiu and J. Yang, *J. Alloys Compd.*, 2017, **695**, 818.

111  F. Shahzad, M. Alhabeb, C. B. Hatter, B. Anasori, S. Man Hong, C. M. Koo and Y. Gogotsi, *Science*, 2016, **353**, 1137.

112  H. B. Wu, J. S. Chen, H. H. Hng and X. W. Lou, *Nanoscale*, 2012, **4**, 2526.

113  J. Jiang, Y. Li, J. Liu, X. Huang, C. Yuan and X. W. Lou, *Adv. Mater.*, 2012, **24**, 5166.

114  Z. Wang, L. Zhou and X. W. Lou, *Adv. Mater.*, 2012, **24**, 1903.

115  D. Xiong, X. Li, Z. Bai and S. Lu, *Small*, 2018, **14**, 1703419.

116  S. Kumar and U. Schwingenschlögl, *Phys. Rev. B*, 2016, **94**, 035405.

117  X. Zhang, X. Zhao, D. Wu, Y. Jing and Z. Zhou, *Nanoscale*, 2015, **7**, 16020–16025.

118  Y. He, M. Zhang, J. Shi, Y. Cen and M. Wu, *J. Phys. Chem. C*, 2019, **123**, 12781–12790.

119  Y. Cheng, L. Wang, Y. Li, Y. Song and Y. Zhang, *J. Phys. Chem. C*, 2019, **123**, 15629–15636.

120  H. Weng, A. Ranjbar, Y. Liang, Z. Song, M. Khazaei, S. Yunoki, M. Arai, Y. Kawazoe, Z. Fang and X. Dai, *Phys. Rev. B: Condens. Matter Mater. Phys.*, 2015, **92**, 075436.

121  M. Khazaei, A. Ranjbar, M. Arai and S. Yunoki, *Phys. Rev. B*, 2016, **94**, 125152.

122  C. Si, K. H. Jin, J. Zhou, Z. M. Sun and F. Liu, *Nano Lett.*, 2016, **16**, 6584–6591.

123 C. Si, J. You, W. Shi, J. Zhou and Z. Sun, *J. Mater. Chem. C*, 2016, **4**, 11524–11529.

124 Y. Liang, M. Khazaei, A. Ranjbar, M. Arai, S. Yunoki, Y. Kawazoe, H. Weng and Z. Fang, *Phys. Rev. B*, 2017, **96**, 195414.

125 G. Gao, G. Ding, J. Li, K. Yao, M. Wu and M. Qian, *Nanoscale*, 2016, **8**, 8986–8994.

126 C. Si, J. Zhou and Z. Sun, *ACS Appl. Mater. Interfaces*, 2015, **7**, 17510–17515.

127 G. Wang, *J. Phys. Chem. C*, 2016, **120**, 18850–18857.

128 L. Hu, X. Wu and J. Yang, *Nanoscale*, 2016, **8**, 12939–12945.

129 J. He, P. Lyu and P. Nachtigall, *J. Mater. Chem. C*, 2016, **4**, 11143–11149.

130 J. He, P. Lyu, L. Z. Sun, A. M. Garcia and P. Nachtigall, *J. Mater. Chem. C*, 2016, **4**, 6500–6509.

131 G. Centi and S. Perathoner, *Catal. Today*, 2010, **150**, 151–162.

132 A. P. Upadhyay, D. K. Behara, G. P. Sharma, A. Bajpai, N. Sharac, R. Ragan, R. G. Pala and S. Sivakumar, *ACS Appl. Mater. Interfaces*, 2013, **5**, 9554–9562.

133 S. Cheng, H. Liu and B. E. Logan, *Environ. Sci. Technol.*, 2006, **40**, 364–369.

134 B. Z. Zhan, M. A. White, T. K. Sham, J. A. Pincock, R. J. Doucet, K. R. Rao, K. N. Robertson and T. S. Cameron, *J. Am. Chem. Soc.*, 2003, **125**, 2195–2199.

135 M. Yagi, E. Tomita, S. Sakita, T. Kuwabara and K. Nagai, *J. Phys. Chem. B*, 2005, **109**, 21489–21491.

136 Y. Zheng, Y. Jiao, Y. Zhu, Q. Cai, A. Vasileff, L. H. Li, Y. Han, Y. Chen and S. Z. Qiao, *J. Am. Chem. Soc.*, 2017, **139**, 3336–3339.

137 H. Yu, L. Shang, T. Bian, R. Shi, G. I. Waterhouse, Y. Zhao, C. Zhou, L. Z. Wu, C. H. Tung and T. Zhang, *Adv. Mater.*, 2016, **28**, 5080–5086.

138 J. Tian, R. Ning, Q. Liu, A. M. Asiri, A. O. Al-Youbi and X. Sun, *ACS Appl. Mater. Interfaces*, 2014, **6**, 1011–1017.

139 S. Zhao, H. Yin, L. Du, L. He, K. Zhao, L. Chang, G. Yin, H. Zhao, S. Liu and Z. Tang, *ACS Nano*, 2014, **8**, 12660–12668.

140 A. Aijaz, N. Fujiwara and Q. Xu, *J. Am. Chem. Soc.*, 2014, **136**, 6790–6793.

141 T. Y. Ma, S. Dai, M. Jaroniec and S. Z. Qiao, *J. Am. Chem. Soc.*, 2014, **136**, 13925–13931.

142 B. Y. Xia, Y. Yan, N. Li, H. B. Wu, X. W. Lou and X. Wang, *Nat. Energy*, 2016, **1**, 15006.

143 S. Zhao, Y. Wang, J. Dong, C. T. He, H. Yin, P. An, K. Zhao, X. Zhang, C. Gao, L. Zhang, J. Lv, J. Wang, J. Zhang, A. M. Khattak, N. A. Khan, Z. Wei, J. Zhang, S. Liu, H. Zhao and Z. Tang, *Nat. Energy*, 2016, **1**, 16184.

144 F. Song and X. Hu, *Nat. Commun.*, 2014, **5**, 4477.

145 J. Jiang, A. Zhang, L. Li and L. Ai, *J. Power Sources*, 2015, **278**, 445–451.

146 Z. Lu, W. Xu, W. Zhu, Q. Yang, X. Lei, J. Liu, Y. Li, X. Sun and X. Duan, *Chem. Commun.*, 2014, **50**, 6479–6482.

147 F. Song and X. Hu, *J. Am. Chem. Soc.*, 2014, **136**, 16481–16484.

148 T. Y. Ma, J. L. Cao, M. Jaroniec and S. Z. Qiao, *Angew. Chem., Int. Ed.*, 2016, **55**, 1138–1142.

149 L. Zhao, B. Dong, S. Li, L. Zhou, L. Lai, Z. Wang, S. Zhao, M. Han, K. Gao, M. Lu, X. Xie, B. Chen, Z. Liu, X. Wang, H. Zhang, H. Li, J. Liu, H. Zhang, X. Huang and W. Huang, *ACS Nano*, 2017, **11**, 5800–5807.

150 H. Zou, B. He, P. Kuang, J. Yu and K. Fan, *ACS Appl. Mater. Interfaces*, 2018, **10**, 22311–22319.

151 M. Yu, S. Zhou, Z. Wang, J. Zhao and J. Qiu, *Nano Energy*, 2018, **44**, 181–190.

152 Z. W. Seh, K. D. Fredrickson, B. Anasori, J. Kibsgaard, A. L. Strickler, M. R. Lukatskaya, Y. Gogotsi, T. F. Jaramillo and A. Vojvodic, *ACS Energy Lett.*, 2016, **1**, 589–594.

153 X. Wu, Z. Wang, M. Yu, L. Xiu and J. Qiu, *Adv. Energy Mater.*, 2017, **29**, 1607017.

154 L. Xiu, Z. Wang, M. Yu, X. Wu and J. Qiu, *ACS Nano*, 2018, **12**, 8017–8028.

155 C. F. Du, K. N. Dinh, Q. Liang, Y. Zheng, Y. Luo, J. Zhang and Q. Yan, *Adv. Energy Mater.*, 2018, **8**, 1801127.

156 J. Ran, G. Gao, F. T. Li, T. Y. Ma, A. Du and S. Z. Qiao, *Nat. Commun.*, 2017, **8**, 13907.

157 X. An, W. Wang, J. Wang, H. Duan, J. Shi and X. Yu, *Phys. Chem. Chem. Phys.*, 2018, **20**, 11405–11411.

158 S. Cao, B. Shen, T. Tong, J. Fu and J. Yu, *Adv. Sci. News*, 2018, **28**, 1800136.

159 H. Brix and H. H. Schierup, *Ambio*, 1989, **18**, 100–107.

160 Y. C. Lee and J. W. Yang, *J. Ind. Eng. Chem.*, 2012, **18**, 1178–1185.

161 Q. Zhang, Y. Li, Q. Yang, H. Chen, X. Chen, T. Jiao and Q. Peng, *J. Hazard. Mater.*, 2018, **342**, 732–740.

162 Y. Ying, Y. Liu, X. Wang, Y. Mao, W. Cao, P. Hu and X. Peng, *ACS Appl. Mater. Interfaces*, 2015, **7**, 1795–1803.

163 A. Shahzad, K. Rasool, W. Miran, M. Nawaz, J. Jang, K. A. Mahmoud and D. S. Lee, *ACS Sustainable Chem. Eng.*, 2017, **5**, 11481–11488.

164 Z. Wei, Z. Peigen, T. Wubian, Q. Xia, Z. Yamei and M. Zheng, *Mater. Chem. Phys.*, 2017, **206**, 270–276.

165 Q. Zhang, J. Teng, G. Zou, Q. Peng, Q. Du, T. Jiao and J. Xiang, *Nanoscale*, 2016, **8**, 7085–7093.

166 Y.-J. Zhang, J.-H. Lan, L. Wang, Q.-Y. Wu, C.-Z. Wang, T. Bo, Z.-F. Chai and W.-Q. Shi, *J. Hazard. Mater.*, 2016, **308**, 402–410.

167 L. Wang, L. Yuan, K. Chen, Y. Zhang, Q. Deng, S. Du, Q. Huang, L. Zheng, J. Zhang and Z. Chai, *ACS Appl. Mater. Interfaces*, 2016, **8**, 16396–16403.

168 K. Rasool, M. Helal, A. Ali, C. E. Ren, Y. Gogotsi and K. A. Mahmoud, *ACS Nano*, 2016, **10**, 3674–3684.

169 K. Rasool, K. A. Mahmoud, D. J. Johnson, M. Helal, G. R. Berdiyorov and Y. Gogotsi, *Sci. Rep.*, 2017, **7**, 1598.

170 M. Yousef Elahi, A. A. Khodadadi and Y. Mortazavi, *J. Electrochem. Soc.*, 2014, **161**, B81–B87.

171 Y. Wang, H. Li and J. Kong, *Sens. Actuators, B*, 2014, **193**, 708–714.

172 K.-A. N. Duerloo, M. T. Ong and E. J. Reed, *J. Phys. Chem. Lett.*, 2012, **3**, 2871–2876.

173 C. N. Rao, K. Gopalakrishnan and U. Maitra, *ACS Appl. Mater. Interfaces*, 2015, **7**, 7809–7832.

174 J. F. Wu, M. Q. Xu and G. C. Zhao, *Electrochem. Commun.*, 2010, **12**, 175–177.

175 G. X. Wang, W. J. Bao, J. Wang, Q. Q. Lu and X. H. Xia, *Electrochem. Commun.*, 2013, **35**, 146–148.

176 Y. H. Zhang, Y. B. Chen, K. G. Zhou, C. H. Liu, J. Zeng, H. L. Zhang and Y. Peng, *Nanotechnology*, 2009, **20**, 185504.

177 C. C. Mayorga-Martinez, Z. Sofer and M. Pumera, *Angew. Chem., Int. Ed.*, 2015, **54**, 14317–14320.

178 M. Gautam and A. H. Jayatissa, *Solid-State Electron.*, 2012, **78**, 159–165.

179 R. Jain, R. Sharma, R. K. Yadav and R. Shrivastava, *J. Electrochem. Soc.*, 2013, **160**, H179–H184.

180 H. Liu, C. Duan, C. Yang, W. Shen, F. Wang and Z. Zhu, *Sens. Actuators, B*, 2015, **218**, 60–66.

181 C. Li, O. Dag, T. D. Dao, T. Nagao, Y. Sakamoto, T. Kimura, O. Terasaki and Y. Yamauchi, *Nat. Commun.*, 2015, **6**, 6608.

182 A. Samphao, P. Butmee, J. Jitcharoen, L. Svorc, G. Raber and K. Kalcher, *Talanta*, 2015, **142**, 35–42.

183 R. Devasenathipathy, V. Mani, S. M. Chen, S. T. Huang, T. T. Huang, C. M. Lin, K. Y. Hwa, T. Y. Chen and B. J. Chen, *Enzyme Microb. Technol.*, 2015, **78**, 40–45.

184 Q. Xu, S. X. Gu, L. Jin, Y. Zhou, Z. Yang, W. Wang and X. Hu, *Sens. Actuators, B*, 2014, **190**, 562–569.

185 A. D. Chowdhury, R. Gangopadhyay and A. De, *Sens. Actuators, B*, 2014, **190**, 348–356.

186 G. X. Zhong, W. X. Zhang, Y. M. Sun, Y. Q. Wei, Y. Lei, H. P. Peng, A. L. Liu, Y. Z. Chen and X. H. Lin, *Sens. Actuators, B*, 2015, **212**, 72–77.

187 Q. Wang, F. Min and J. Zhu, *Mater. Lett.*, 2013, **91**, 9–11.

188 R. B. Rakhi, P. Nayak, C. Xia and H. N. Alshareef, *Sci. Rep.*, 2016, **6**, 36422.

189 B. Xiao, Y. Li, X. Yu and J. Cheng, *Sens. Actuators, B*, 2016, **235**, 103–109.

190 S. J. Kim, H. J. Koh, C. E. Ren, O. Kwon, K. Maleski, S. Y. Cho, B. Anasori, C. K. Kim, Y. K. Choi, J. Kim, Y. Gogotsi and H. T. Jung, *ACS Nano*, 2018, **12**, 986–993.

191 E. Lee, A. VahidMohammadi, B. C. Prorok, Y. S. Yoon, M. Beidaghi and D. J. Kim, *ACS Appl. Mater. Interfaces*, 2017, **9**, 37184–37190.

192 A. C. Rajan, A. Mishra, S. Satsangi, R. Vaish, H. Mizuseki, K.-R. Lee and A. K. Singh, *Chem. Mater.*, 2018, **30**, 4031–4038.